Sedimentary Geology 464 (2024) 106618

Contents lists available at ScienceDirect

Sedimentary Geology

journal homepage: www.elsevier.com/locate/sedgeo

A Cretaceous siliceous sinter in NE China: Sedimentological and geochemical constraints on its genesis

Yaxian You [a,b], Huaguo Wen [a,b,*], Lianchao Luo [a,b,*], Kathleen A. Campbell [c], Diego M. Guido [d], Enrico Capezzuoli [e], Zhipeng Lu [a,b], Lei Du [f], Yunbao Yang [g]

[a] State Key Laboratory of Oil and Gas Reservoir Geology and Exploitation, Chengdu University of Technology, Chengdu 610059, China
[b] Institute of Sedimentary Geology, Chengdu University of Technology, Chengdu 610059, China
[c] School of Environment & Te Ao Mārama – Centre for Fundamental Inquiry, Faculty of Science, The University of Auckland, Private Bag 92019, Auckland 1142, New Zealand
[d] CONICET and Facultad de Ciencias Naturales y Museo, Universidad Nacional de La Plata, Instituto de Recursos Minerales (INREMI), Calle 64 y 120, La Plata 1900, Argentina
[e] Department of Earth Sciences, University of Florence, Florence 50121, Italy
[f] Beijing Dadi Hi-tech Geological Exploration Company Limited, Beijing 100040, China
[g] The First Institute of Geology Exploration of Heilongjiang Province, Mudanjiang 157000, China

ARTICLE INFO

Article history:
Received 28 December 2023
Received in revised form 29 February 2024
Accepted 29 February 2024
Available online 06 March 2024

Editor: Dr. Brian Jones

Keywords:
Cretaceous
Sinter
Geothermal reservoir
$^{87}Sr/^{86}Sr$
Rare-earth elements

ABSTRACT

Phanerozoic sinter deposits have been reported globally, with their identification mainly based on sedimentological, petrological, and mineralogical studies. In this study, a detailed geochemical investigation, combined with sedimentological characterization, was conducted on the Wugonglilu siliceous deposit, a Cretaceous (106 Ma) sinter in NE China, to examine its genesis. The deposit is inferred as a siliceous hot spring deposit (sinter) owing to its geological setting in an epithermal gold-mining district, its morphologically variable microbial textures typical of subaerial sinters, and nearly pure silica composition. Three lithofacies were recognized in this study, including laminated to thinly bedded sinter, silica-cemented breccia, and epithermal vein, which represent deposits from three contrasting hydrothermal environments. The $^{87}Sr/^{86}Sr$ ratios of the sinter are similar to the bedrock through which the geothermal fluids passed, namely the Upper Triassic Dajiahe Formation (T_3dj), a marine siliceous rock unit, and the Lower Cretaceous Datashanlinchang Formation (K_1d), a rhyolite unit. Results indicate that both underlying units are possible Sr sources of the silica in the Wugonglilu sinter. The REE + Y (rare-earth elements and yttrium) patterns of the sinter exhibit significant variability, primarily due to terrestrial detrital contamination. Differential REE + Y contamination by terrestrial detritus was striking in the white and dark laminae/beds of the laminated to thinly bedded sinter. The white laminae/beds, generally less contaminated, were probably formed during the dry season, whereas the dark laminae/beds exhibiting greater detrital contamination were likely formed during the wet season. When excluding the samples strongly contaminated by detritus, the sinter exhibits Y anomalies comparable to Post-Archean Australian Shale (PAAS), and to the adjacent underlying K_1d rhyolite and T_3dj siliceous rock samples, indicating that these anomalies were not inherited from rocks dominating the reservoirs. Furthermore, the sinter shows a $(Ce/Ce^*)_N$ range close to that of the underlying marine siliceous rock and rhyolite samples, reflecting that the $(Ce/Ce^*)_N$ of the sinter is largely inherited from the reservoir rock(s). The overall REE + Y patterns of the sinter range from nearly flat to LREE-depleted, similar to some samples of the K_1d rhyolite and T_3dj siliceous rock units. However, most samples of the K_1d rhyolite and T_3dj siliceous rock display $(Pr/Tb)_N$ and $(Pr/Yb)_N$ higher than many studied sinter samples. This is likely because of the formation of strong HREE–carbonate complexes during groundwater migration. Based on these results, a generalized formation model of the studied sinter system was constructed. This study suggests that integrated sedimentological and geochemical investigations can aid in interpreting the genesis of sinter deposits, in particular the link between sinter deposits and corresponding reservoir rocks.

1. Introduction

Sinter is a common silica deposit formed in terrestrial hot springs at Earth's surface, derived from the precipitation of non-crystalline opaline silica mainly caused by the rapid cooling of near-neutral pH, alkali-chloride, SiO_2-rich hydrothermal fluids (e.g., Fournier and Rowe,

* Corresponding authors at: State Key Laboratory of Oil and Gas Reservoir Geology, Chengdu University of Technology, Chengdu 610059, China.
E-mail addresses: wenhuaguo08@cdut.edu.cn (H. Wen), luolianchao@cdut.edu.cn (L. Luo).

https://doi.org/10.1016/j.sedgeo.2024.106618

1966; Fournier, 1985a). Sinter deposits have been recognized in many modern hot spring systems, such as Yellowstone National Park (USA) (e.g., Walter, 1976a; Guidry and Chafetz, 2002; Churchill et al., 2021), the Taupo and Coromandel volcanic zone (New Zealand) (e.g., Jones et al., 1997a; Campbell et al., 2001; Lynne and Campbell, 2003; Drake et al., 2014; Hamilton et al., 2019a), Tengchong and Dagejia (China) (e.g., Jones and Peng, 2015; Wang et al., 2019), Iceland (e.g., Konhauser et al., 2001; Tobler et al., 2008; Jones and Renaut, 2010) and El Tatio (Chile) (e.g., Jones and Renaut, 1997; Fernandez-Turiel et al., 2005). However, Mesozoic–Paleozoic sinter deposits have only been reported from a few places, such as in the Jurassic Deseado Massif (Argentina) (e.g., Guido et al., 2010; Guido and Campbell, 2011; Guido and Campbell, 2014), the Devonian Rhynie and Windyfield cherts (Scotland) (e.g., Channing et al., 2007; Krings, 2021), and the Devonian Drummond Basin (Australia) (e.g., Walter et al., 1996; Walter et al., 1998). The limited reports of older Phanerozoic sinter deposits may be attributed to the fact that the sedimentary and biofacies characteristics of sinter can easily be destroyed by taphonomic, diagenetic and erosional processes (e.g., Lynne et al., 2007; Campbell et al., 2015a; Lynne, 2015; Watts-Henwood et al., 2017; Campbell et al., 2019).

Previous studies of Phanerozoic sinter deposits have mainly focused on their sedimentological, petrological, and mineralogical characteristics (e.g., Jones and Renaut, 2003; Uysal et al., 2011; Guido and Campbell, 2014; Campbell et al., 2015a; Guido et al., 2019; Hamilton et al., 2019b), while in-depth geochemical characterization has been less commonly undertaken (Uysal et al., 2011; Hamilton et al., 2019b; Churchill et al., 2021). Geochemical characteristics, such as $^{87}Sr/^{86}Sr$ and REE + Y (rare-earth elements and yttrium) of hot spring waters, are indicative of the fluid origin and the type of reservoir rock (e.g., Möller et al., 2004; Huenges, 2010; Loges et al., 2012a; Kobare et al., 2023). Siliceous sinter is deposited from hot springs; therefore, it likely inherits some geochemical signatures from the thermal fluids (e.g., Uysal et al., 2011; Feng et al., 2014) and thus may provide valuable information about fluid origins, reservoir rock (Luo et al., 2024) and related upwelling conduits (Brogi et al., 2023). Additionally, depositional processes (e.g., the influx of detritus) may affect the geochemical characteristics of sinter (Luo et al., 2024), which may be influenced by seasonal changes in the depositional system. Hence, geochemical characterization of sinter may also be useful in the interpretation of sinter depositional environments.

This study investigated the sedimentological and geochemical signatures of an inferred Cretaceous sinter deposit (i.e., the so-called Cretaceous Sipingshan Formation siliceous rocks) at Wugonglilu, Heilongjiang Province, NE China (Fig. 1A). The aim of this study is to determine the fluid origin of the sinter and to unravel its depositional environment(s) and genesis. Based on this integrated sedimentological

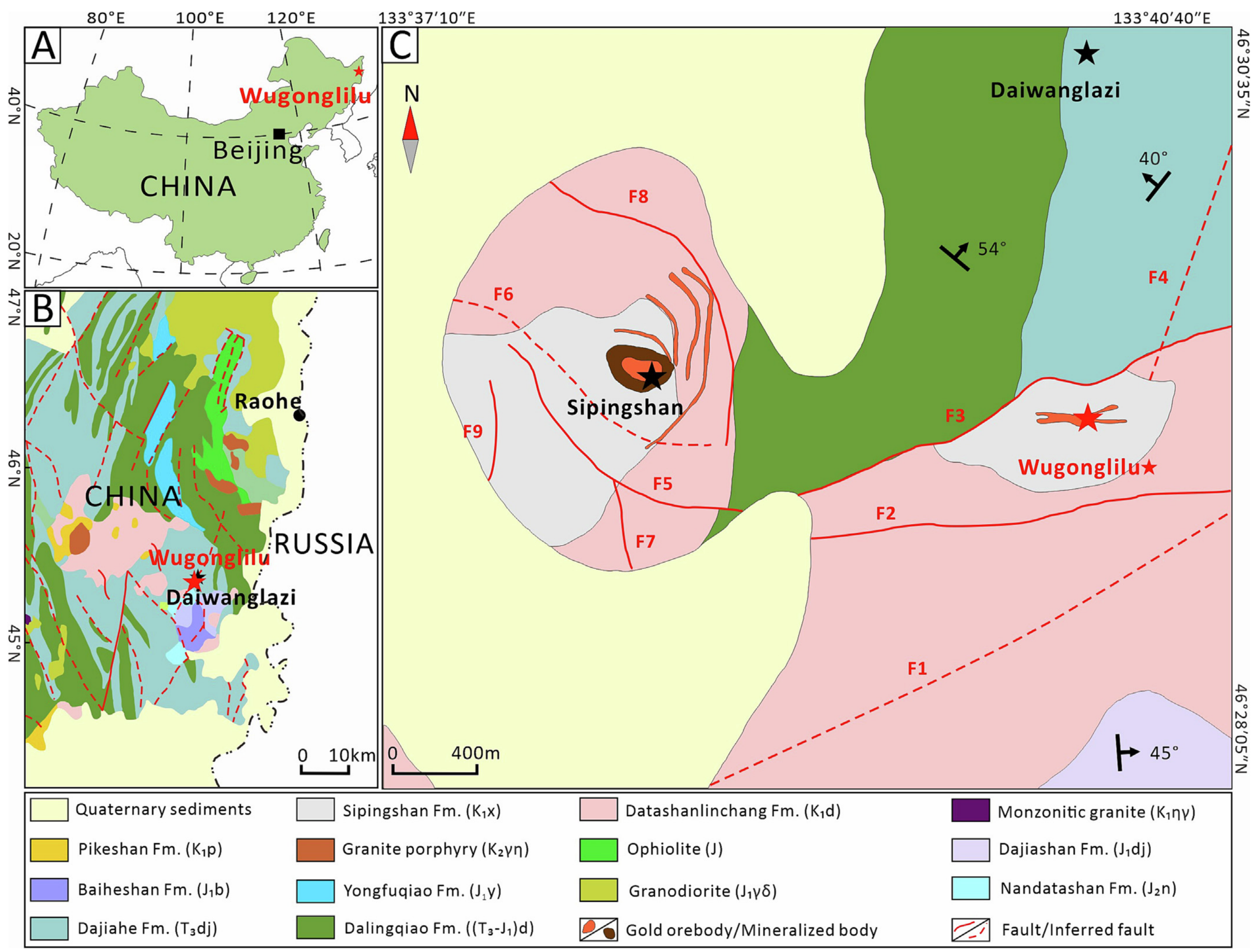

Fig. 1. (A) Geographic location of Wugonglilu, China. (B) Simplified geological map of the study area (modified after Ren et al. (2020) and Zhang (2014)). Sequence is composed of the Upper Triassic Dajiahe Formation (T_3dj) marine siliceous strata; the Upper Triassic–Lower Jurassic Dalingqiao Formation ((T_3-J_1)d) silty slate and argillaceous siltstone; the Middle Jurassic Nandatashan Formation (J_2n) rhyolite, dacite and breccia tuff; the Lower Jurassic Yongfuqiao Formation (J_1y) sandstone, Baiheshan Formation (J_1b) silty slate and sandstone, and Dajiashan Formation (J_1dj) conglomerates; the Lower Cretaceous Pikeshan Formation (K_1p) rhyolite, Datashanlinchang Formation (K_1d) rhyolite and Sipingshan Formation (K_1x) sinter and Quaternary sediments. (C) Detailed geological map of Wugonglilu and surrounding area (modified after Zhang (2009)). ⅄ represents the strike and dip of the rocks.

and geochemical investigation, a formation model of the studied sinter was also constructed. The findings may aid in interpreting the sedimentological and geochemical signatures of fossil sinter deposits and revealing the relationship between sinter deposits and corresponding reservoir rock(s).

2. General background

The study area, Wugonglilu (133°39′55″ E, 46°29′12″ N) (Fig. 1), also named Daiwanglazi (e.g., Wang et al., 2022; Han et al., 2023), is situated in the southeastern part of the Sipingshan Gold Field, which is located on the eastern margin of the Wandashan Terrane, NE China (e.g., Zhang, 2014; Han et al., 2023). Deposits cropping out in the Wugonglilu area (Xu et al., 2005; Zhang, 2009, 2014; Huang et al., 2010; Sun et al., 2012; Quan and Dong, 2013; Zhang et al., 2013; Wang et al., 2022; Han et al., 2023; He et al., 2023) mainly comprise: the Upper Triassic Dajiahe Formation (T_3dj) marine siliceous rocks; the Upper Triassic–Lower Jurassic Dalingqiao Formation ((T_3-J_1)d) silty slate and argillaceous siltstone; the Lower Jurassic (Dajiashan Formation, J_1dj) conglomerates; the Lower Cretaceous Datashanlinchang Formation (K_1d) rhyolite; the Lower Cretaceous Sipingshan Formation (K_1x), including sandstone, as well as silica-cemented breccia and siliceous rock (i.e., bedded/laminated sinter), and Quaternary sediments (Fig. 1B, C). A series of near E–W (F1, F2 and F3) and nearby NNE tensional faults (F4) occur in the study area (Fig. 1C), which were initiated by volcanic activity, and controlled hydrothermal upwelling during the early Cretaceous period (e.g., Zhang, 2009, 2014). Furthermore, the Cretaceous paleoclimate in this area was characterized by a warm-temperate, humid climate with distinctly seasonal variations (e.g., Cheng and Ge, 2008; Yang et al., 2013a).

Based on previous studies of the lithology of the Cretaceous Sipingshan Formation (K_1x), these deposits were divided into three parts: a sandstone-dominated lower part, a silica-cemented breccia-dominated middle part, and an upper part dominated by laminated to thinly bedded sinter (e.g., Zhang, 2009; Huang et al., 2010; Sun et al., 2012; Han et al., 2023). These deposits directly accumulated on the southwestern slopes and within topographic depressions of volcanic domes represented by the Datashanlinchang Formation (K_1d) rhyolite, and developed at both Sipingshan and Wugonglilu (e.g., Sun et al., 2000; Quan and Dong, 2013). Typically, the sandstone part constitutes a nearly 15-m-thick succession and occurs below a 10 to over 50-m-thick succession consisting of silica-cemented breccia (e.g., Sun et al., 2000). The sandstone strata are likely lacustrine deposits, accompanied by common carbonized wood, silicified wood, and fine-grained pyrite (e.g., Sun et al., 2012; Quan and Dong, 2013). In contrast, the silica-cemented breccia, a matrix-supported rock, is interpreted as being associated with a hydrothermal explosion. This is evidenced by the disorderly arranged, sub-rounded to sub-angular clasts (such as rhyolite and silicified sandstone) of up to 3 cm in diameter (e.g., Sun et al., 2000; Huang et al., 2010; Sun et al., 2012). The bedded sinter is characterized by alternating dark and white laminated to thinly bedded horizons (herein termed laminae/beds or laminated/bedded), with the continuity of the layers obscured in some places. Geochronological investigations on the pyrite in the Sipingshan Formation (K_1x) sinter reveal a depositional age of around 106 ± 3 Ma (Han et al., 2023) and therefore the Wugonglilu sinter is an Early Cretaceous deposit. Mining activity at Wugonglilu and Sipingshan has been extensive, now limiting the available outcrops. At Wugonglilu and Sipingshan, the bedded sinter is now only found at the edges of mining pits and has a thickness of <20 m, but prior to mining its areal extent was approximately 0.5 km^2 (Zhang, 2014). In addition to the laminated to bedded sinter, silica-cemented breccia and millimeter- to meter-scale siliceous veins of the Sipingshan Formation are well exposed. Therefore, several stratigraphically related siliceous deposits were examined in this study, including the upper bedded sinter, the lower silica-cemented breccia, and the cross-cutting siliceous veins.

3. Methods

The distribution of the laminated/bedded sinter and siliceous veins at Wugonglilu was mapped in the field and samples were collected for further laboratory study. Approximately 80 samples, including both the sinter and adjacent bedrock units (i.e. rhyolite and marine siliceous strata) were collected. Detailed petrological and mineralogical characteristics of the sinter were investigated from 65 thin sections using a digital camera (Nikon DS-Ri1, Japan) attached to a transmitted light optical microscope (Nikon Eclipse E400 POL, Japan) at the University of Auckland, New Zealand. Thirty-nine samples were selected for analysis of trace elements (REE + Y, Sr, Rb, Zr, Th, Mn, Sc and Ba) and ^{87}Sr/^{86}Sr. Prior to geochemical analysis, samples were powdered using an agate mortar and pestle. A microdrill was also utilized to collect small samples from the alternating white and dark laminae/beds of the bedded sinter and the powdered samples were used to examine their geochemical differences.

For trace element analysis, sample powder (40 mg) was dissolved using 0.5 ml high-purity HNO_3 and 1 ml high-purity HF in a Teflon beaker placed in a 190 °C oven. The dissolved samples were then transferred to 100 ml Teflon bottles, and a Rh internal standard was added. These solutions were further diluted by adding 2 % HNO_3 until 100 g. Analysis was conducted at Beijing Createch Testing Technology Co., Ltd. (China) utilizing ICP-MS (PlasmaQuant MS, Analytik Jena, Germany), following a standardized procedure and operating conditions described in Eggins et al. (1997). Analytical precision is better than 5 % for REE, Rb, Sr, Cs, Ba, U, Th, Pb, Zr and Hf, and 10 % for other trace elements.

For Sr isotopic analysis, samples were digested using 1.5 ml of 4 N HNO_3 and 3 ml of 4 N HF in a Teflon cup on a hot plate for seven days. The dissolved samples were then evaporated to dryness, followed by the addition of 1 ml of 6 N HCl to ensure complete digestion. After the HCl solution had evaporated, the samples were further treated with 1 ml of 4 N HNO_3 and then processed through polypropylene columns with Sr-specific resin to separate Sr. Analysis was carried out at the State Key Laboratory of Oil and Gas Reservoir Geology (Chengdu University of Technology) using a TIMS Triton plus (Thermo Fisher Scientific, America). All the Sr isotopic data were acquired in the static collection mode. The obtained ^{87}Sr/^{86}Sr values were adjusted by normalizing them to ^{86}Sr/^{88}Sr = 0.1194. The NIST standard reference NBS-987 (200 ppm) Sr standard yielded ^{87}Sr/^{86}Sr = 0.71027052 ± 0.0000132 (2SD, n = 2) during the measurement period. A total of 120 Sr isotopic ratios were collected for each sample to ensure sufficient precision.

REE + Y data were normalized to Post-Archean Australian Shale (PAAS) (Taylor and McLennan, 1985) for comparative studies, and the normalized values were expressed as the element plus suffix "N". The ratios of $(Pr/Yb)_{SN}$, $(Pr/Tb)_{SN}$ and $(Tb/Yb)_{SN}$ were used to evaluate relative enrichments of the LREE (from La to Nd), MREE (from Sm to Dy), and HREE (from Er to Lu) fractions. Ce, Eu and Y anomalies were calculated algebraically as follows (Lawrence et al., 2006; Zhao et al., 2022):

$$\text{Ce anomaly}: (Ce/Ce^*)_N = Ce_N/(Pr_N \times (Pr_N/Nd_N)) \quad (1)$$

$$\text{Eu anomaly}: (Eu/Eu^*)_N = Eu_N/\left(Sm_N{}^2 \times Tb_N\right)^{1/3} \quad (2)$$

$$\text{Y anomaly}: \text{Y/Ho} \quad (3)$$

4. Results

4.1. Lithofacies

Sinter and sinter-associated deposits (Figs. 2 to 4) were recognized in the Sipingshan Formation at Wugonglilu based on field sedimentological characterization and laboratory petrological and mineralogical examination. They are laminated to thinly bedded sinter, sinter-

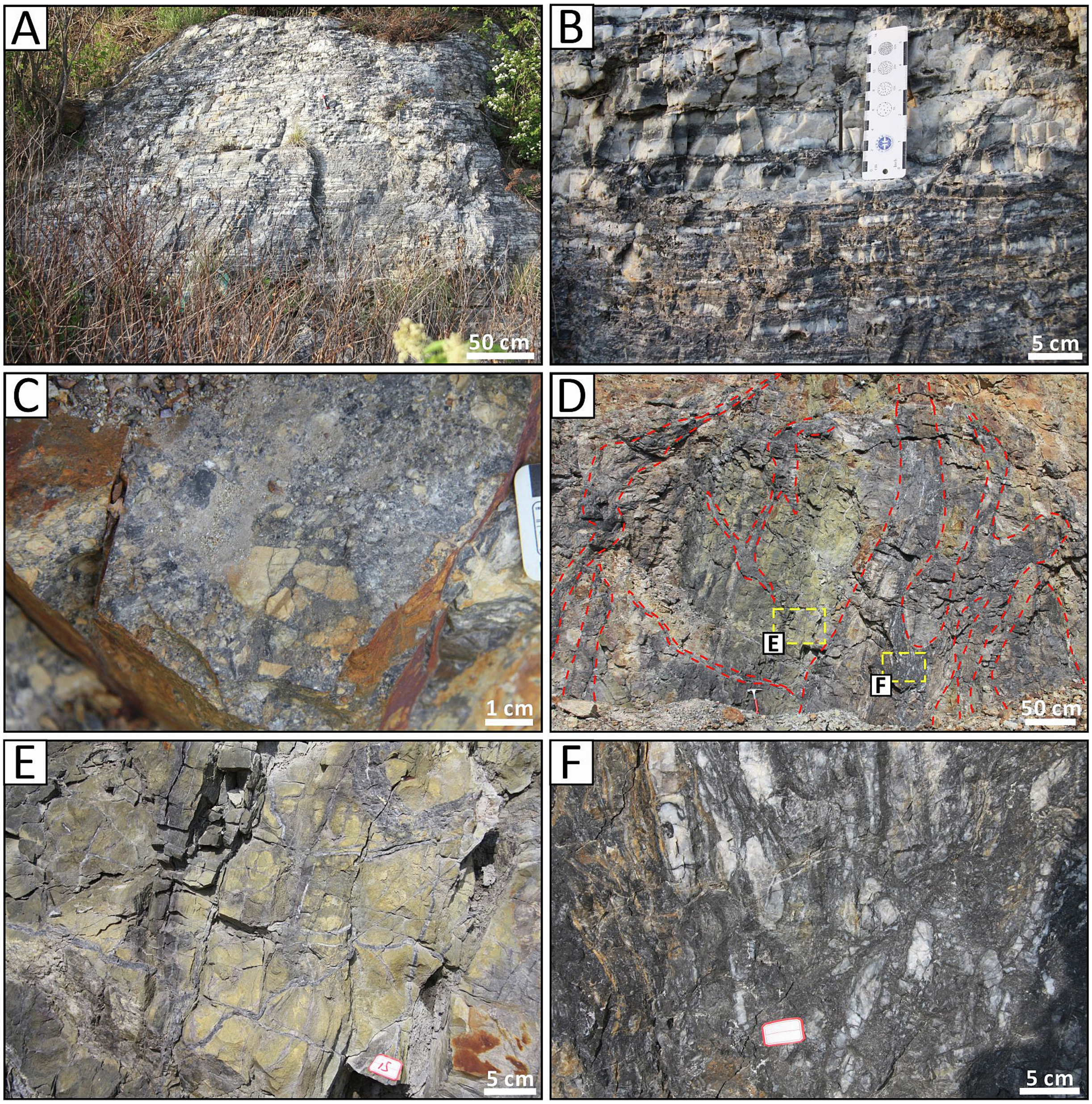

Fig. 2. Field photos of the laminated to thinly bedded sinter, silica-cemented breccia and epithermal veins from the Wugonglilu study area. (A) Outcrop of the laminated to thinly bedded sinter, showing alternating dark and white layers, nearly parallel in orientation. (B) Striking alternation of wavy white and dark horizons characterized by varying thicknesses, from 1 cm to 5 cm for the white layers and 0.5 cm to 3 cm for the dark laminae/beds. (C) Outcrop of silica-cemented breccia consisting of millimeter to centimeter diameter, sub-rounded to sub-angular fragments of siliceous rock (i.e. sinter), rhyolite and siltstone. (D) Vertical to lateral epithermal veins cutting through the pre-existing rhyolite. (E) Enlarged view of the yellow box in Panel D. Local small epithermal veins cross-cut the rhyolite and can intersect other veins. (F) Detail of (D) showing brecciated and recrystallized quartz from within veins.

cemented breccia, and epithermal veins. In this section, lithofacies are first described, and then comparisons are made between the studied Chinese deposits and siliceous hydrothermal deposits from the literature, in order to aid in a refined interpretation of the depositional setting.

4.1.1. Laminated to thinly bedded sinter

4.1.1.1. Description. Sinter is the most common lithofacies at Wugonglilu (Figs. 2A, B and 3). The remaining field outcrops of the sinter in the studied area have a maximum thickness of approximately 20 m, forming even today an extensive deposit that spans over 300 m in the North–South direction and nearly 200 m in the East–West direction. The sinter surfaces are now exposed directly to the present-day land surface, with no subsequent rock layers currently preserved above them. Visually striking alternation of white and dark laminae/beds characterizes the sinter, and it has a shallow dip (1° to ~10°) to the northeast. The sinter layers vary significantly in thickness, ranging from <1 cm to >5 cm thick. Many geologists define laminae and beds in terms of thickness, with laminae being <1 cm thick and beds >1 cm thick, respectively (e.g., McKee and Weir, 1953; Kelley, 1956). Thus, 'laminated to thinly bedded sinter' (abbreviated to 'laminated/bedded') is the terminology used in this study to accurately describe the thickness characteristics of the dark and white layers of the Wugonglilu sinter. The layers of laminated/bedded sinter are wavy to parallel, typically 0.5 to 5 cm thick. Notably, the white layers are typically thicker than the dark layers (Fig. 2B). The former usually range from 1 cm to 5 cm in thickness, while the latter are typically between 0.5 cm and 3 cm thick. However, in few places, thick dark layers (1 to 3 cm thick) intercalated with thin white layers (typically <1.5 cm in thickness) were also observed (Fig. 2B). Additionally, many of these layers exhibit significant lateral changes in thickness and can be interrupted by adjacent layers with a different

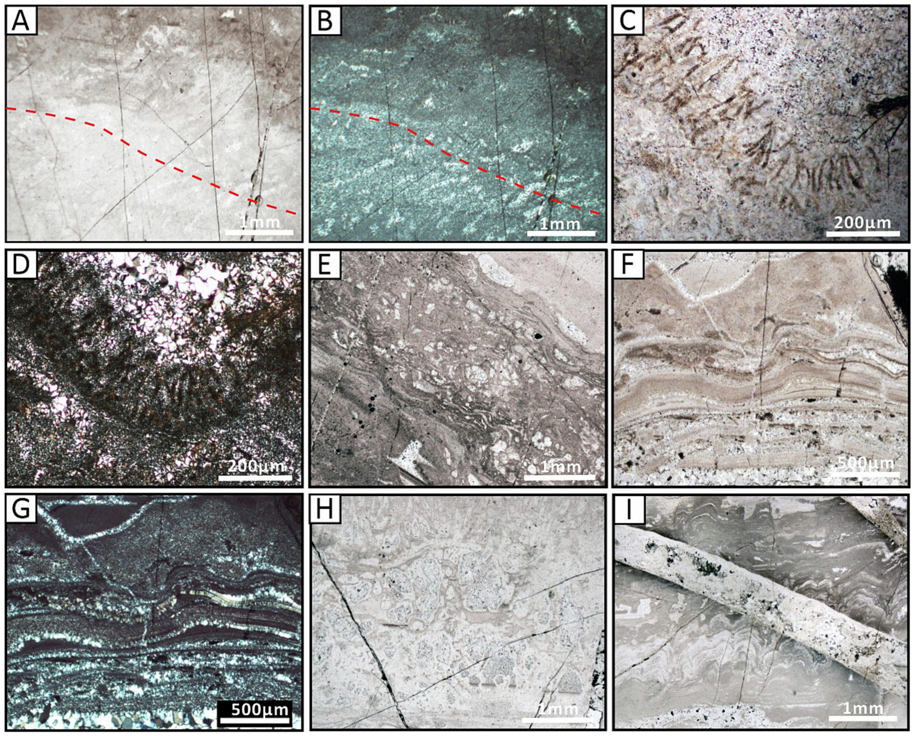

Fig. 3. Photomicrographs (plane polarized light, PL; cross-polarized light, CPL) of laminated to thinly bedded sinter (A–I). (A) Dark laminae (above the red dashed line) and white laminae (in plane polarized light). Dark laminae contain microbial fabrics (domal and columnar microfabrics), while the white laminae are devoid of microbe-associated structures. (B) Same view as (A), but under cross-polarized light (CPL), showing that both the dark and white laminae are mainly composed of cryptocrystalline quartz. Plane-polarized (C) and cross-polarized (D) views of the sinter with preserved palisade fabrics, containing a sequence of densely packed, subvertical to vertical, tubular filamentous microbes (lengths: 50 to 500 μm; diameters: near 20 μm) that are predominantly composed of cryptocrystalline and microcrystalline (<40 μm) quartz. (E) Microstromatolite with wavy micro-laminae, containing inferred bubbles and geopetals. (F) Microstromatolite textures display flat to wavy thin layers under plane polarized light (PL). (G) Microtexture of the layers under CPL reveals alternating laminae of cryptocrystalline quartz and microcrystalline quartz (<100 μm). (H) Small columnar/digitate and spicular textural features of microstromatolite. (I) Microstromatolite with cumulate to pseudocolumnar morphologies.

color (Fig. 2B). Thin-section analysis revealed that the laminated/bedded sinter is predominantly composed of cryptocrystalline to microcrystalline (<50 μm) quartz (Fig. 3B, D, G, I), and the microstructures of the overlying and underlying laminae show obvious differences (Fig. 3A, B). In particular, with respect to the dark layers, microbial textures were observed, including filaments, microstromatolites, and clotted fabrics, whereas the white laminae and thin beds did not exhibit microbial microfabrics nor microstructures (Figs. 3 and A2). Filamentous microfossils (Figs. 3C, D and A2) are quite common in the dark laminae/beds and range from 50 to 500 μm in length and can be up to almost 20 μm in diameter. The filaments occur individually, or collectively to form vertical micro-pillar clusters, or palisade fabrics. Microstromatolites (Fig. 3A, B, E–I) are less common than the filamentous structures. The microstromatolites commonly comprise flat or wavy laminae (Fig. 3E, F, G), but some domical, columnar/digitate, cumulate to pseudocolumnar, and even spicular morphologies have also been noted (Figs. 3A, B, H, I and A2B). Each micro-lamina within a microstromatolite consists of cryptocrystalline quartz or microcrystalline (typically 1 to 50 μm) quartz with laminae alternating between the two sizes in some samples. No obvious filamentous microbes were noted in thin section analysis of the microstromatolites; however, curved laminae with voids (inferred to be bubbles associated with microbial photosynthesis; Campbell et al., 2001; Bosak et al., 2009) and geopetals (Fig. 3E) are present in some examples. Furthermore, a mm-scale stratigraphic transition from palisade fabrics to digitate, spicular features is also present in some samples. Clotted fabric was only detected in the dark laminae/beds of some samples, and measured diameters of individual clots are from 100 to 400 μm (Fig. 3H, I). The clotted siliceous material is typically composed of cryptocrystalline quartz (<1 μm), and, in some cases, clots are bound together, generating net-like structures. Irregular pores (of a wide range in sizes, from dozens of μm to 0.5 mm) are well developed in the dark laminae and thin beds, especially in those with microstromatolites and clots, with most filled with clear microcrystalline to mesocrystalline (200 to 250 μm) quartz cements. These silica cements are characterized by isopachous textures, forming single or multiple cement rims growing around clots. Comparatively, the white laminae/beds are dense, exhibiting only a few pores. Late diagenetic fractures are prevalent in both the dark and white laminae/beds, and these are commonly filled with microcrystalline to mesocrystalline (50 to 400 μm) quartz, similar to the fill of many cavities in the laminated/bedded sinter.

4.1.1.2. Interpretation. Laminated to thinly bedded sinter is a very common lithofacies in sinter deposits (e.g., Guido and Campbell, 2009; Guido and Campbell, 2014; Jones and Peng, 2015; Campbell et al., 2019; Hamilton et al., 2019c; Campbell et al., 2020), especially those from low-relief slope environments (Campbell et al., 2019; Campbell et al., 2020). This is mostly the case of the studied sinter, as it shows very flat and laterally extensive laminae and thin beds. Laminations in sinter can be interpreted to be controlled by variations in microbial activity (Konhauser et al., 2001; Jones and Peng, 2015). In the studied sinter, the dark laminae/beds yield an abundance of microbial textures and are thus considered to have formed during periods when microorganisms were able to keep pace with silicification, while the white laminae were largely formed in periods when microbial growth was slower (Konhauser et al., 2001; Jones and Peng, 2015). Moreover, laminations in sinter also can be controlled by physical processes. These physical processes affect the formation of sinter laminae on a sinter apron by controlling changes in rates of silica precipitation (e.g., Walter, 1976a; Farmer and Des Marais, 1994; Cady and Farmer, 1996). A high deposition rate of sinter is related to high fluid discharge and/or duration, and therefore thick sinter layers will be formed.

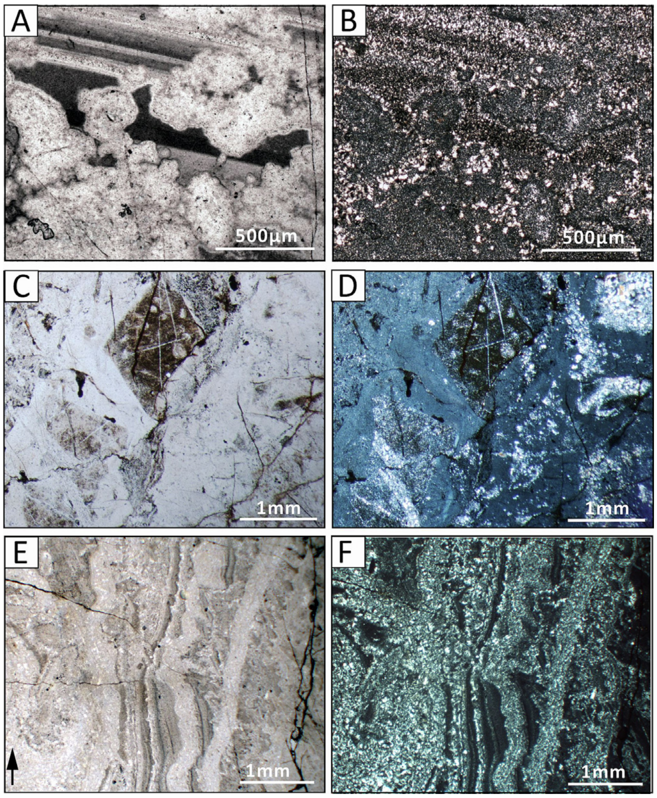

Fig. 4. (A) μm-Scale sinter clot (100 to 400 μm), bound together and obscuring laminations. (B) Cross-polarized view of (A) illustrating clot composition of cryptocrystalline quartz, with a rim of microcrystalline quartz (<40 μm), distinguishing it from cryptocrystalline quartz. (C) Plane-polarized views of a silica-cemented breccia. Subrounded to sub-angular clasts consist of siliceous rock, rhyolite, siltstone, claystone. (D) Cross-polarized views of a silica-cemented breccia with matrix mainly composed of microcrystalline (<100 μm) to cryptocrystalline quartz. (E) Epithermal vein example under PL and CPL (F), characterized by the cyclic alternation of laminae comprising cryptocrystalline quartz and microcrystalline quartz (<100 μm). Dark arrow indicates the extended orientation of veins.

Palisades and microstromatolites of varied morphologies, which are the two most common microbial fabrics in the studied laminated/bedded sinter, are known from low- and middle-temperature environments of terrestrial geothermal systems, respectively. In particular, palisade fabrics are mainly reported from sinter terraces of the distal apron (<40 °C thermal fluid temperatures), typically meters to tens of meters from vent areas, and in low-relief flats with extensive thin sheets of thermal spring outflow (e.g., Cady and Farmer, 1996; Lynne, 2012; Campbell et al., 2015b; Hamilton et al., 2019c; Campbell et al., 2020). In addition, microstromatolites can be observed in calm, hot spring pools (~40–60 °C) in the middle sinter apron, meters to tens of meters from vent areas, and can grow and flatten out at the air–water interface (e.g., Walter, 1976a; Cady and Farmer, 1996; Jones et al., 2005; Hamilton et al., 2019a, 2019c). Certain micromorphological features (e.g., Awramik and Grey, 2005; Van Kranendonk, 2011), including domical and columnar/digitate microstromatolites (Fig. 3A, B), as well as bubbles (Fig. 3E) associated with microbial mats, may indicate the biogenicity of fossil microstromatolites. Additionally, observations of irregular pores (Fig. 3E) within microstromatolites can be interpreted as fenestral fabrics, indicative of microbial degassing.

4.1.2. Silica-cemented breccia

4.1.2.1. Description. This lithofacies, where present, occurred beneath the laminated to thinly bedded sinter. It is mainly composed of matrix-supported, poorly sorted, sub-rounded to sub-angular clasts, ranging in size from several millimeters to centimeters in diameter (Figs. 2C and 4C, D). The gravel-sized clasts were found to be dominantly composed of fragments of silica sinter, rhyolite, siltstone, and claystone. The matrix filling the spaces around the clasts is cryptocrystalline to microcrystalline silica cement, and the individual microcrystalline quartz crystals (1 to 70 μm) have irregular boundaries. In some examples, these quartz crystals tend to cluster, showing a characteristic thin rim of spherulitic, microcrystalline quartz (5 to 10 μm), which is followed inward by quartz with an increasing crystal size up to nearly 70 μm (Fig. 4D). There were commonly two stages to the silica cementation: the first was dominantly cryptocrystalline silica, whereas the second consisted of intergrown quartz microcrystals.

4.1.2.2. Interpretation. The gravel-sized clasts of the silica-cemented breccia were formed either by the erosion of parent rocks and subsequent transport and deposition of clasts in the study area, or by sudden, steam-heated hydrothermal eruptions that brecciated earlier-formed deposits, including sinter (e.g., Jones et al., 1997b; Browne and Lawless, 2001; Renaut et al., 2002; Renaut et al., 2017).

4.1.3. Epithermal veins

4.1.3.1. Description. Abundant vertically-to-laterally extensive, distributed silica veins that cross-cut pre-existing rhyolites were observed in the mining pit (Fig. 2D–F) and are here referred to as epithermal veins. The thickness of the veins varies from a few millimeters to several decimeters, and they can intersect each other, forming vein networks (Fig. 2E). The veins extend laterally and vertically for tens of meters, along which their lengths and thicknesses may vary greatly. As shown in Fig. 2D, the outcropping veins form a tree-shaped system of dykes that thin upward and host silica-rich infills. Thin-section observations reveal that the epithermal veins consist of cryptocrystalline to microcrystalline quartz (1 to 50 μm), and pyrite was identified in places. The veins typically feature crustiform bands characterized by cyclic alternation of laminae composed of quartz with different crystal sizes (Fig. 4E, F). In some examples, a later group of fractures (mainly filled with nearly 300 μm mesocrystalline quartz) cross-cuts all other geological features.

4.1.3.2. Interpretation. Epithermal veins are abundant in hydrothermal systems (e.g., Simmons et al., 2005; Rowland and Simmons, 2012; Sillitoe, 2015; Hamilton et al., 2019c; Ünal Ercan et al., 2022). They are precipitated by subsurface thermal fluids injecting unfilled fractures and form mainly during pulses in the upwelling of thermal fluids. Thus, they record migration directions of hydrothermal fluids and are late-stage products of hydrothermal activities (Ünal Ercan et al., 2022). Epithermal veins are shallow subsurface epithermal deposits that are commonly associated with subaerial geothermal systems and low-sulfidation epithermal gold–silver deposits (e.g., Simmons et al., 2005; Davies et al., 2008; Hamilton et al., 2019a). Similar to many low-sulfidation epithermal systems, the formation of the Wugonglilu epithermal veins was largely influenced by fault activity, which fractured earlier-formed deposits, channeling thermal fluids stored in deep-seated hydrothermal reservoirs and serving as main conduits for thermal fluid upwelling.

4.2. Sr and Rb concentrations and $^{87}Sr/^{86}Sr$ geochemistry

Rb and Sr concentrations, as well as $^{87}Sr/^{86}Sr$ measurements from representative laminated/bedded sinter, silica-cemented breccia and epithermal vein samples, together with samples from adjacent bedrock (Datashanlinchang Formation (K_1d) rhyolite and Dajiahe Formation (T_3dj) marine siliceous rock) are presented in Table 1 and Figs. 5 and 6. The laminated/bedded sinter displays relatively uniform $^{87}Sr/^{86}Sr$ ratios between 0.709944 and 0.711678, and a wide range of Sr and Rb concentrations ranging from 2.44 to 35.57 μg g^{-1} (commonly <10 μg g^{-1}) and 1.3 to 12.64 μg g^{-1} (commonly <3 μg g^{-1}), respectively. In addition, the measured $^{87}Sr/^{86}Sr$ ratio of a silica-

Table 1
$^{87}Sr/^{86}Sr$ values and trace element concentrations (μg g^{-1}) of the samples from Wugonglilu. b.d. = below detection limit. See Table A1 for more details.

Sample	Note	$^{87}Sr/^{86}Sr$	Error (2σ)	Sc (μg g^{-1})	Mn (μg g^{-1})	Rb (μg g^{-1})	Sr (μg g^{-1})	Y (μg g^{-1})	Zr (μg g^{-1})	Ba (μg g^{-1})	La (μg g^{-1})	Ce (μg g^{-1})	Pr (μg g^{-1})	Nd (μg g^{-1})	Sm (μg g^{-1})	Eu (μg g^{-1})	Gd (μg g^{-1})	Tb (μg g^{-1})
S1	White laminae/beds of the	0.710900	6.48E−05	0.21	5.39	2.02	4.76	0.20	0.46	17.21	0.02	0.04	0.01	0.02	0.01	0.003	b.d.	b.d.
S2	K_1x laminated to thinly	0.711430	6.68E−06	0.34	5.99	2.10	3.98	0.62	7.01	30.78	0.58	1.04	0.11	0.34	0.07	0.02	0.06	0.01
S3	bedded sinter	0.711028	5.92E−05	0.18	2.48	2.25	5.77	0.23	0.87	59.67	0.04	0.07	0.01	0.03	0.01	0.01	0.01	b.d.
S4		0.710994	2.84E−05	0.21	2.64	1.59	3.45	0.23	0.90	15.85	0.03	0.08	b.d.	0.02	0.01	0.003	0.01	b.d.
S5		0.710962	2.28E−05	0.21	3.03	2.29	4.57	0.23	0.79	24.24	0.05	0.09	0.01	0.04	0.01	0.01	0.01	b.d.
S6		0.711169	2.12E−05	0.22	1.73	3.55	7.78	0.29	1.99	42.83	0.05	0.10	0.01	0.05	0.01	0.01	0.01	b.d.
S7		0.710565	8.40E−06	0.21	8.10	2.92	8.47	0.32	2.79	39.33	0.08	0.16	0.02	0.07	0.02	0.01	0.02	0.004
S8		0.711139	5.79E−06	0.25	3.25	3.03	4.77	0.21	2.96	32.72	0.38	0.77	0.08	0.28	0.04	0.01	0.03	0.01
S9		0.711175	3.37E−05	0.20	6.83	1.55	2.99	0.30	1.55	18.48	0.02	0.05	0.01	0.02	0.01	0.005	0.02	0.003
S10		0.710957	5.36E−05	0.15	0.97	1.49	3.52	0.21	0.94	20.58	0.02	0.03	b.d.	0.01	b.d.	0.004	0.01	b.d.
S11		0.711190	4.96E−05	0.13	1.23	1.30	2.44	0.19	0.42	10.02	0.03	0.05	0.01	0.02	b.d.	b.d.	0.01	b.d.
S12	Dark laminae/beds of the	0.709944	3.00E−05	0.19	2.12	2.71	8.05	0.26	1.79	60.71	0.05	0.10	0.01	0.04	0.01	0.01	0.01	b.d.
S13	K_1x laminated to thinly	0.711580	2.86E−05	0.43	19.71	8.45	10.53	0.51	7.31	91.09	2.03	4.20	0.47	1.65	0.28	0.04	0.14	0.02
S14	bedded sinter	0.711041	3.55E−05	0.27	5.22	2.96	6.20	0.62	6.42	64.19	0.11	0.24	0.02	0.09	0.03	0.02	0.05	0.01
S15		0.710576	1.68E−05	0.36	28.85	2.77	5.44	0.62	9.48	57.09	0.33	0.77	0.07	0.27	0.06	0.02	0.07	0.01
S16		0.711312	5.83E−05	0.26	12.01	3.18	6.60	0.30	1.31	40.80	0.19	0.41	0.04	0.16	0.03	0.01	0.03	0.004
S17		0.711678	8.03E−06	0.25	7.10	3.02	4.82	0.26	3.17	39.49	0.68	1.33	0.15	0.54	0.11	0.02	0.06	0.01
S18		0.710141	4.19E−06	0.94	197.09	12.64	35.57	2.31	23.44	302.76	3.99	8.63	0.92	3.11	0.60	0.12	0.56	0.08
S19		0.711528	1.11E−05	0.65	20.77	6.04	9.23	1.19	22.11	100.82	1.40	2.75	0.28	0.93	0.16	0.03	0.12	0.03
S20		0.710717	8.06E−06	0.65	13.71	13.12	13.47	1.00	20.32	121.35	2.51	4.92	0.48	1.43	0.24	0.04	0.15	0.03
S21		0.710703	2.62E−05	0.27	3.58	1.75	4.02	0.52	5.03	39.05	0.08	0.15	0.02	0.07	0.03	0.01	0.04	0.01
S22		0.711236	1.06E−06	0.20	8.17	1.69	3.92	0.22	2.84	34.38	0.08	0.20	0.01	0.07	0.02	0.01	0.02	0.01
S23		0.711354	5.46E−05	0.29	1.48	1.71	3.92	0.55	5.67	42.66	0.04	0.09	0.01	0.04	0.02	0.01	0.04	0.01
C	K_1x silica-cemented breccia	0.712163	1.06E−05	1.57	12.63	5.33	11.09	4.85	108.38	174.16	3.91	7.03	0.75	2.41	0.50	0.10	0.51	0.11
V1	K_1x epithermal veins	0.711683	8.04E−06	0.42	17.84	8.07	15.96	0.84	5.68	57.27	3.03	5.94	0.62	2.00	0.38	0.07	0.24	0.03
V2		0.715055	5.61E−06	0.92	10.33	27.63	30.30	3.04	30.75	98.67	6.86	13.03	1.38	4.52	0.86	0.16	0.64	0.10
V3		0.709929	8.52E−06	0.72	7.78	10.30	33.49	1.52	14.08	103.25	10.42	19.07	2.22	7.44	1.28	0.20	0.57	0.06
V4		0.709991	2.94E−06	0.68	9.59	6.50	21.11	2.36	14.07	88.61	8.50	17.53	1.94	6.68	1.27	0.22	0.80	0.10
V5		0.710816	4.57E−06	0.98	11.38	5.06	42.30	2.52	17.71	100.50	19.16	36.03	3.75	11.72	2.43	0.44	1.42	0.14
R1	K_1d rhyolite	0.719809	8.04E−06	2.29	16.79	58.04	29.58	5.46	46.59	106.37	9.37	19.11	2.27	7.92	1.47	0.24	0.99	0.16
R2		0.714484	3.02E−06	1.38	13.75	41.17	22.02	3.30	21.84	81.03	3.13	6.45	0.69	2.32	0.50	0.09	0.47	0.09
R3		0.713901	4.65E−06	2.48	9.65	7.89	17.30	12.30	104.44	52.23	11.09	20.17	2.13	6.75	1.34	0.23	1.43	0.30
M1	T_3dj marine siliceous rock	0.711509	1.80E−05	2.36	3.70	3.75	9.09	13.08	71.39	74.78	3.71	7.47	0.89	3.04	0.63	0.18	1.13	0.28
M2		0.711055	2.48E−05	2.09	4.30	10.51	40.38	3.77	13.57	172.19	4.46	10.45	1.17	4.44	0.91	0.20	0.79	0.12
M3		0.711940	5.79E−05	1.36	2.66	3.74	8.87	6.38	39.04	66.17	1.15	2.65	0.39	1.22	0.27	0.09	0.54	0.13
M4		0.716553	9.81E−06	3.70	28.42	22.51	28.83	7.50	31.23	186.69	9.41	19.42	2.51	8.98	2.02	0.40	1.53	0.23
M5		0.711248	5.09E−05	1.07	2.73	5.06	16.31	1.65	5.93	181.20	1.23	3.16	0.40	1.32	0.26	0.09	0.27	0.05
M6		0.710331	3.78E−05	2.19	19.81	7.21	37.43	4.69	21.34	225.09	11.05	18.55	2.52	9.56	1.74	0.30	0.88	0.14
M7		0.709893	7.20E−05	2.29	18.26	6.83	60.22	4.36	18.92	195.45	16.81	27.80	4.17	16.59	2.98	0.44	1.25	0.16

(continued on next page)

Table 1 (*continued*)

Sample	Note	Dy (μg g^{-1})	Ho (μg g^{-1})	Er (μg g^{-1})	Tm (μg g^{-1})	Yb (μg g^{-1})	Lu (μg g^{-1})	Pb (μg g^{-1})	Th (μg g^{-1})	U (μg g^{-1})	Ba/Eu	Y/Ho	ΣREE	$(Ce/Ce^*)_N$	$(Eu/Eu^*)_N$	$(Pr/Yb)_N$	$(Pr/Tb)_N$	$(Tb/Yb)_N$
S1	White laminae/beds of the	0.004	b.d.	b.d.	b.d.	b.d.	b.d.	0.23	b.d.	0.01	5061	245.25	0.11	0.83	3.29	0.85	0.58	1.45
S2	K_1x laminated to thinly	0.09	0.02	0.07	0.01	0.07	0.01	2.28	0.83	0.25	1673	32.06	2.50	0.98	1.21	0.45	0.64	0.71
S3	bedded sinter	0.01	b.d.	0.01	b.d.	0.01	b.d.	0.31	b.d.	0.05	5611	103.91	0.21	1.11	6.14	0.45	0.38	1.16
S4		0.01	b.d.	0.01	b.d.	0.01	b.d.	0.31	b.d.	0.06	4662	113.10	0.17	1.94	2.54	0.23	0.25	0.94
S5		0.01	b.d.	0.01	b.d.	0.01	b.d.	0.37	b.d.	0.05	4312	103.73	0.24	1.06	2.62	0.49	0.43	1.14
S6		0.02	0.004	0.01	b.d.	0.01	b.d.	0.53	b.d.	0.19	5408	68.05	0.29	1.18	3.05	0.24	0.33	0.73
S7		0.03	0.01	0.02	b.d.	0.02	b.d.	1.04	b.d.	0.49	4075	59.30	0.47	1.00	2.22	0.35	0.38	0.93
S8		0.03	0.004	0.02	0.005	0.02	0.01	1.30	b.d.	0.21	2415	47.80	1.68	1.05	1.62	1.14	1.26	0.90
S9		0.02	0.004	0.02	b.d.	0.01	b.d.	1.22	b.d.	0.10	3826	67.14	0.19	1.10	2.30	0.13	0.15	0.88
S10		0.01	b.d.	0.01	b.d.	b.d.	b.d.	1.43	b.d.	0.08	5138	134.13	0.10	0.99	4.21	0.30	0.27	1.09
S11		0.01	b.d.	b.d.	b.d.	b.d.	b.d.	0.25	b.d.	0.04	4524	242.00	0.12	0.99	2.47	0.90	0.56	1.60
S12	Dark laminae/beds of the	0.02	0.003	0.01	b.d.	0.01	b.d.	1.13	b.d.	0.04	5714	86.00	0.29	0.98	4.74	0.44	0.47	0.93
S13	K_1x laminated to thinly	0.09	0.01	0.05	0.01	0.06	0.01	4.87	1.16	0.40	2091	34.59	9.08	0.97	1.00	2.49	2.23	1.11
S14	bedded sinter	0.08	0.02	0.06	0.01	0.06	0.01	4.61	b.d.	0.23	3777	37.22	0.79	1.15	2.18	0.13	0.19	0.65
S15		0.09	0.02	0.07	0.01	0.08	0.01	3.56	0.81	0.32	2943	33.46	1.89	1.29	1.32	0.28	0.41	0.68
S16		0.02	0.004	0.01	b.d.	0.01	b.d.	3.87	b.d.	0.07	3878	70.57	0.94	1.14	1.72	1.05	0.91	1.16
S17		0.04	0.01	0.02	0.01	0.03	0.01	3.51	b.d.	0.25	1772	39.77	3.00	1.03	1.27	1.67	1.51	1.11
S18		0.43	0.08	0.24	0.04	0.25	0.04	11.40	1.88	2.44	2449	28.10	19.09	0.99	1.05	1.16	0.95	1.21
S19		0.18	0.04	0.14	0.02	0.17	0.03	5.85	1.18	0.98	3032	29.67	6.29	1.00	0.97	0.53	0.89	0.59
S20		0.16	0.03	0.11	0.02	0.13	0.02	2.76	1.23	1.68	2781	30.38	10.26	0.95	1.01	1.20	1.56	0.77
S21		0.06	0.01	0.04	0.01	0.05	0.01	4.03	b.d.	0.25	3164	39.89	0.58	1.08	1.79	0.11	0.16	0.70
S22		0.03	0.005	0.02	0.01	0.02	0.01	4.44	b.d.	0.17	3217	46.23	0.52	2.09	1.93	0.22	0.22	1.00
S23		0.06	0.01	0.04	0.01	0.05	0.01	3.86	b.d.	0.27	3579	41.77	0.44	1.12	2.36	0.06	0.11	0.59
C	K_1x silica-cemented breccia	0.77	0.17	0.55	0.09	0.62	0.10	3.43	2.99	1.41	1817	28.70	17.63	0.93	0.82	0.38	0.58	0.66
V1	K_1x epithermal veins	0.15	0.03	0.08	0.01	0.09	0.01	2.29	1.98	0.38	793	29.80	12.68	0.95	1.15	2.28	1.71	1.33
V2		0.55	0.11	0.33	0.05	0.31	0.05	4.86	2.86	0.82	634	27.76	28.93	0.96	0.98	1.40	1.21	1.16
V3		0.30	0.06	0.17	0.03	0.17	0.03	5.88	3.99	0.85	507	27.07	42.03	0.89	1.13	4.04	2.96	1.36
V4		0.49	0.09	0.25	0.04	0.24	0.04	6.11	3.29	1.03	394	26.37	38.18	0.96	1.08	2.59	1.66	1.56
V5		0.57	0.10	0.28	0.04	0.27	0.04	14.79	5.79	1.75	227	25.96	76.40	0.93	1.24	4.35	2.32	1.87
R1	K_1d rhyolite	0.92	0.19	0.58	0.09	0.55	0.09	3.12	3.34	0.78	442	28.99	43.94	0.91	0.90	1.29	1.24	1.04
R2		0.55	0.11	0.33	0.05	0.29	0.05	3.11	1.69	0.37	887	29.30	15.14	0.96	0.85	0.75	0.66	1.14
R3		1.96	0.44	1.36	0.21	1.39	0.21	6.14	7.55	2.75	227	28.12	49.00	0.92	0.74	0.48	0.61	0.79
M1	T_3dj marine siliceous rock	2.02	0.45	1.44	0.22	1.57	0.23	3.40	3.94	1.23	426	28.80	23.25	0.89	0.97	0.18	0.28	0.64
M2		0.64	0.14	0.42	0.06	0.42	0.06	3.70	1.66	0.32	845	27.87	24.27	1.05	1.16	0.88	0.85	1.03
M3		0.96	0.22	0.70	0.11	0.76	0.12	3.10	2.33	0.69	707	29.06	9.30	0.67	1.15	0.16	0.25	0.64
M4		1.30	0.26	0.76	0.11	0.70	0.11	6.94	2.81	0.78	462	28.44	47.74	0.86	1.09	1.14	0.95	1.19
M5		0.26	0.06	0.18	0.03	0.17	0.02	1.42	0.95	0.16	2094	28.52	7.49	0.81	1.54	0.73	0.72	1.01
M6		0.78	0.17	0.54	0.08	0.53	0.08	9.24	2.38	0.90	741	26.85	46.93	0.86	1.07	1.51	1.61	0.94
M7		0.77	0.17	0.50	0.07	0.50	0.07	9.36	2.14	0.73	444	26.32	72.28	0.82	1.04	2.64	2.32	1.14

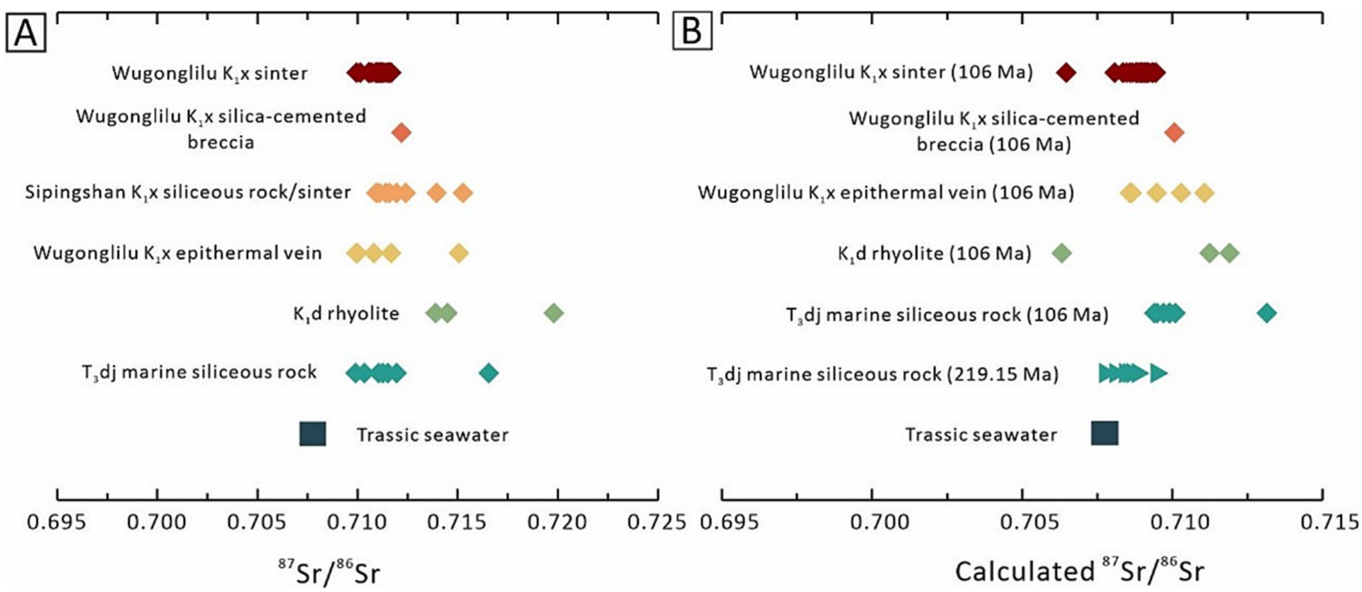

Fig. 5. (A) Measured $^{87}Sr/^{86}Sr$ and (B) calculated $^{87}Sr/^{86}Sr$ data for the studied sinter, compared with $^{87}Sr/^{86}Sr$ signatures of its (potential) reservoir rock(s) and the Sipingshan siliceous rocks. $^{87}Sr/^{86}Sr$ values of the Sipingshan siliceous rocks (Panel A) are from Han et al. (2023). Initial $^{87}Sr/^{86}Sr$ of the Wugonglilu sinter was obtained using a sinter depositional age of 106 Ma (data from Han et al. (2023)), and calculated values were compared with $^{87}Sr/^{86}Sr$ of potential Sr source rocks in the Early Cretaceous (i.e., $^{87}Sr/^{86}Sr_{cre}$). Initial $^{87}Sr/^{86}Sr$ of the T_3dj marine siliceous rocks was obtained by using the median age (219.15 Ma) of the beginning of the Upper Triassic (237 Ma) and the end of the Upper Triassic (201.3 Ma), and then compared with the $^{87}Sr/^{86}Sr$ of the Triassic seawater (the latter from Antonelli et al., 2017).

cemented breccia sample (0.712163) is somewhat higher than the $^{87}Sr/^{86}Sr$ ratio from the laminated/bedded sinter and this sample yields Sr and Rb concentrations of 11.09 and 5.33 μg g^{-1}, respectively. In comparison, epithermal vein samples show similar $^{87}Sr/^{86}Sr$ ratios to the laminated/bedded sinter, varying mainly from 0.709929 to 0.7011683 (with the exception of one sample measuring 0.715055). The Sr and Rb concentrations of epithermal vein samples vary from 15.96 to 42.3 μg g^{-1} and 5.06 to 27.63 μg g^{-1}, respectively.

The K_1d rhyolite exhibits the highest range of $^{87}Sr/^{86}Sr$ values from 0.713901 to 0.719809, and narrow ranges of Sr (17.30 to 29.58 μg g^{-1}) and Rb (7.89 to 58.04 μg g^{-1}) concentrations. The T_3dj marine siliceous rock samples are characterized by relatively uniform $^{87}Sr/^{86}Sr$ ratios from 0.708993 to 0.711940, almost overlapping with the laminated/bedded sinter. However, one sample yielded a significantly higher $^{87}Sr/^{86}Sr$ value (0.716553). The marine siliceous rock samples have a wide range of Sr concentrations (from 9.09 to 60.22 μg g^{-1}) and a relatively narrow range of Rb concentrations (from 3.74 to 22.51 μg g^{-1}).

4.3. REE + Y, Zr, Th, Mn, Sc and Ba signatures

The characteristics of REE + Y and some trace elements (Zr, Th, Mn, Sc and Ba) of the K_1x laminated/bedded sinter, K_1x silica-cemented breccia, K_1x epithermal veins, K_1d rhyolite and T_3dj bedded marine siliceous rocks are shown in Table 1 and Figs. 7–10.

The ΣREE of the Sipingshan Formation (K_1x) laminated/bedded sinter samples ranges from 0.10 to 19.09 μg g^{-1}. However, the white laminae/beds yielded lower ΣREE concentrations (0.10 to 2.50 μg g^{-1}) than the dark laminae/beds (0.29 to 19.09 μg g^{-1}). Their overall REE + Y patterns are highly complex. Flattened REE + Y patterns, LREE-depletion, and LREE-enrichment ($(Pr/Yb)_N = 0.06$ to 2.49; $(Pr/Tb)_N = 0.11$ to 2.23; $(Tb/Yb)_N = 0.59$ to 1.45, respectively) were observed (Fig. 10). Significant positive Eu anomalies existed in the laminated to bedded sinter. Specifically the $(Eu/Eu^*)_N$ values varied from 1.21 to 6.14 in the white laminae/beds, and from 0.97 to 4.74 in the dark laminae/beds. However, $(Ce/Ce^*)_N$ values of the white laminae/beds are in the range of 0.83 to 1.18 (with an exceptional value of 1.94), and those of the dark laminae/beds are in the range of 0.95 to 1.15 (with outliers of 1.29 and 2.09), reflecting no or very weak Ce anomalies. The computed Y/Ho ratios of the white sinter laminae/beds vary from 32.06 to 245.25, whereas the dark laminae/beds show a relatively narrow range of Y/Ho values (Y/Ho = 28.10 to 86.00). Furthermore, Zr, Th, Mn and Sc concentrations in the white laminae/beds range from 0.42 to 7.01 μg g^{-1}, 0.48 to 0.83 μg g^{-1}, 0.97 to 8.10 μg g^{-1} and 0.13 to 0.34 μg g^{-1}, respectively; whereas, those of the dark laminae/beds vary from 1.31 to 23.44 μg g^{-1}, 0.51 to 1.88 μg g^{-1} and 1.48 to 28.85 μg g^{-1} (with an outlier of 197.09 μg g^{-1}), respectively. The laminated/bedded sinter displays a statistically significant, positive linear Th-Zr correlation with 'R^2' of 0.97 in the white laminae/beds and 'R^2' of 0.78 in the dark laminae/beds. Moreover, the Ba concentration of the white laminae and thinly beds is in the range of 10.02 to 59.67 μg g^{-1}, whereas that in the dark laminae/beds exhibits a range of 34.38 to 302.76 μg g^{-1}.

The ΣREE of a K_1x silica-cemented breccia sample is 17.63 μg g^{-1}. The sample shows a flat REE + Y pattern (LREE-depleted relative to HREE and MREE: $(Pr/Yb)_N = 0.38$, $(Pr/Tb)_N = 0.58$ and $(Tb/Yb)_N = 0.66$, respectively), and no significant Eu and Ce anomalies ($(Ce/Ce^*)_N = 0.93$; $(Eu/Eu^*)_N = 0.82$). Its calculated Y/Ho value is 28.70, whereas its Zr, Th, Mn, Sc and Ba contents are 108.38 μg g^{-1}, 2.99 μg g^{-1}, 12.63 μg g^{-1}, 1.57 μg g^{-1} and 174.16 μg g^{-1}, respectively.

The ΣREE of the K_1x epithermal vein samples varies from 12.68 to 76.40 μg g^{-1}. They display high ($(Pr/Yb)_N = 1.40$ to 4.35; $(Pr/Tb)_N = 1.21$ to 2.96) and low $(Tb/Yb)_N$ (0.96 to 1.10) values, suggesting significant LREE enrichment relative to MREE and HREE. Other characteristics are: 1) no striking Ce anomalies ($(Ce/Ce^*)_N$: 0.89 to 0.96); 2) no or very weak Eu anomalies ($(Eu/Eu^*)_N$: 0.98 to 1.24); 3) a narrow range of Y/Ho (25.96 to 29.80) ratios, and 4) wide variations of Ba (57.27 to 103.25 μg g^{-1}), Zr (5.68 to 30.75 μg g^{-1}), Th (1.98 to 5.79 μg g^{-1}), Mn (7.78 to 17.84 μg g^{-1}) and Sc (0.42 to 0.98 μg g^{-1}) concentrations.

The Datashanlinchang Formation (K_1d) rhyolite samples are characterized by 1) high ΣREE values (15.14 to 49.00 μg g^{-1}); 2) $(Pr/Yb)_N$ ranging from 0.48 to 0.75 and $(Pr/Tb)_N = 0.61$ and 0.66; 3) LREE-enrichment relative to MREE and HREE ($(Pr/Yb)_N = 1.29$; $(Pr/Tb)_N = 1.24$); 4) slightly negative Eu anomalies ($(Eu/Eu^*)_N$: 0.74 to 0.90); 5) slightly negative Ce anomalies ($(Ce/Ce^*)_N$: 0.92 to 0.96); 6) quite uniform Y/Ho (28.12 to 29.30) ratios; and 7) wide ranges of Zr (21.84 to 104.44 μg g^{-1}), Th (1.69 to 7.55 μg g^{-1}), Ba (52.23 to 106.37 μg g^{-1}), Mn (9.65 to 16.79 μg g^{-1}) and Sc (1.38 to 2.48 μg g^{-1}) concentrations.

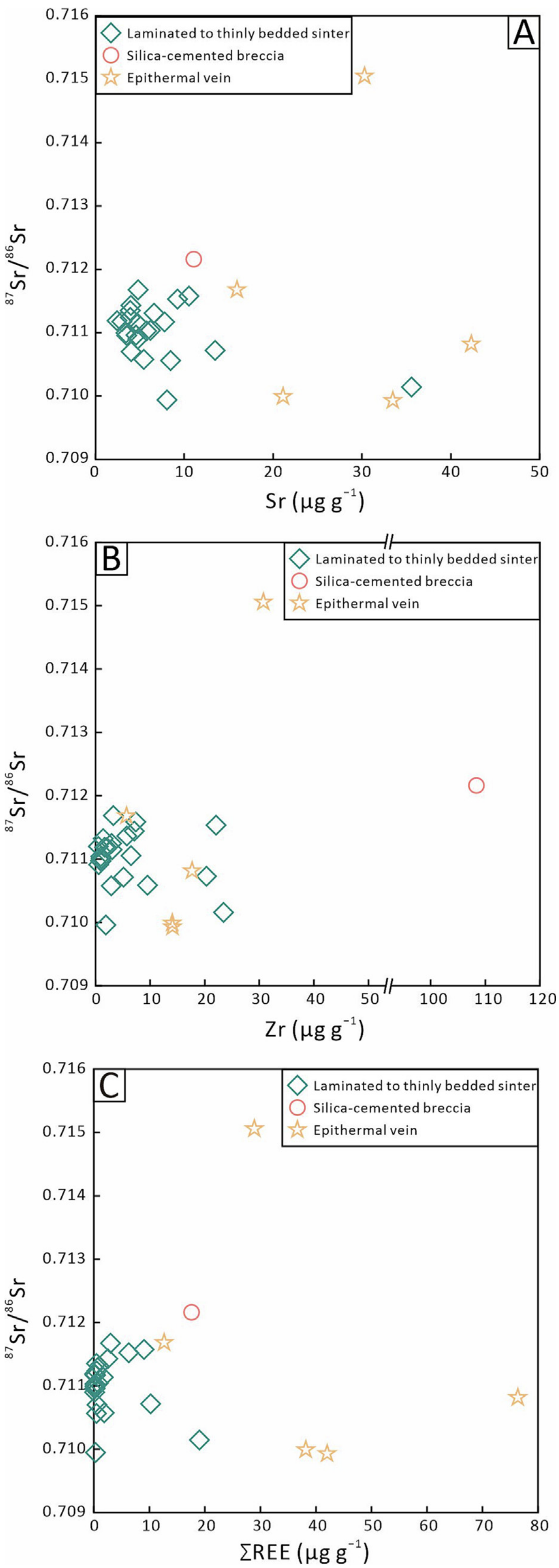

Fig. 6. Plots of (A) $^{87}Sr/^{86}Sr$ ratios vs. Sr contents (μg g^{-1}); (B) $^{87}Sr/^{86}Sr$ ratios vs. Zr contents (μg g^{-1}); and (C) $^{87}Sr/^{86}Sr$ ratios vs. ΣREE (μg g^{-1}) in the studied sinter, silica-cemented breccia and epithermal veins.

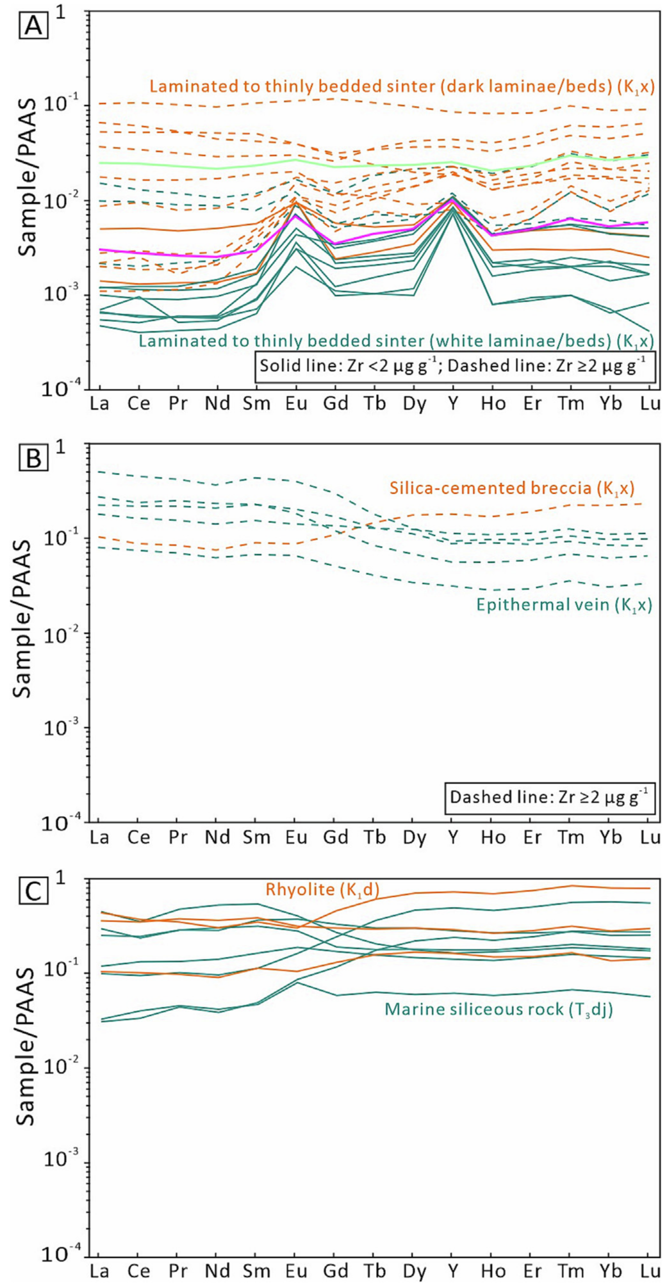

Fig. 7. PAAS-normalized REE + Y patterns for the studied deposits as well as their potential reservoir rock(s) in Wugonglilu. (A) White and dark horizons of the laminated to thinly bedded sinter. Green solid line: mean REE + Y profile line for the white laminae of the sinter; purple solid line: mean REE + Y profile line for the dark laminae of the sinter. (B) Silica-cemented breccia and epithermal veins. (C) Rhyolite and marine siliceous rock. Note that the REE + Y patterns of the sinter with Zr <2 μg g^{-1} (solid line) and Zr ≥2 μg g^{-1} (dashed line) are shown in Panels A and B.

The Dajiahe Formation (T_3dj) bedded marine siliceous rock samples displayed a wide range of ΣREE (7.49 to 72.28 μg g^{-1}) values compared to the laminated to thinly bedded sinter. The bedded marine siliceous samples are LREE-depleted relative to HREE and MREE ($(Pr/Yb)_N$ between 0.16 and 0.88, $(Pr/Tb)_N$ between 0.25 and 0.85, and $(Tb/Yb)_N$ between 0.64 and 1.03), and LREE-enriched relative to HREE ($(Pr/Yb)_N$ = 1.14 and 2.64, $(Pr/Tb)_N$ = 0.95 and 2.32, and $(Tb/Yb)_N$ = 0.94 and 1.19). The marine siliceous rocks also had no or very weak Ce anomalies ($(Ce/Ce^*)_N$: 0.81 to 1.05, with an outlier value of 0.67), and no significant Eu anomalies ($(Eu/Eu^*)_N$: 0.97 to 1.16, with an exception value of 1.54). Their Y/Ho ratios are very uniform, from 26.32 to 29.06. In addition, their Zr, Th, Mn, Sc and Ba contents

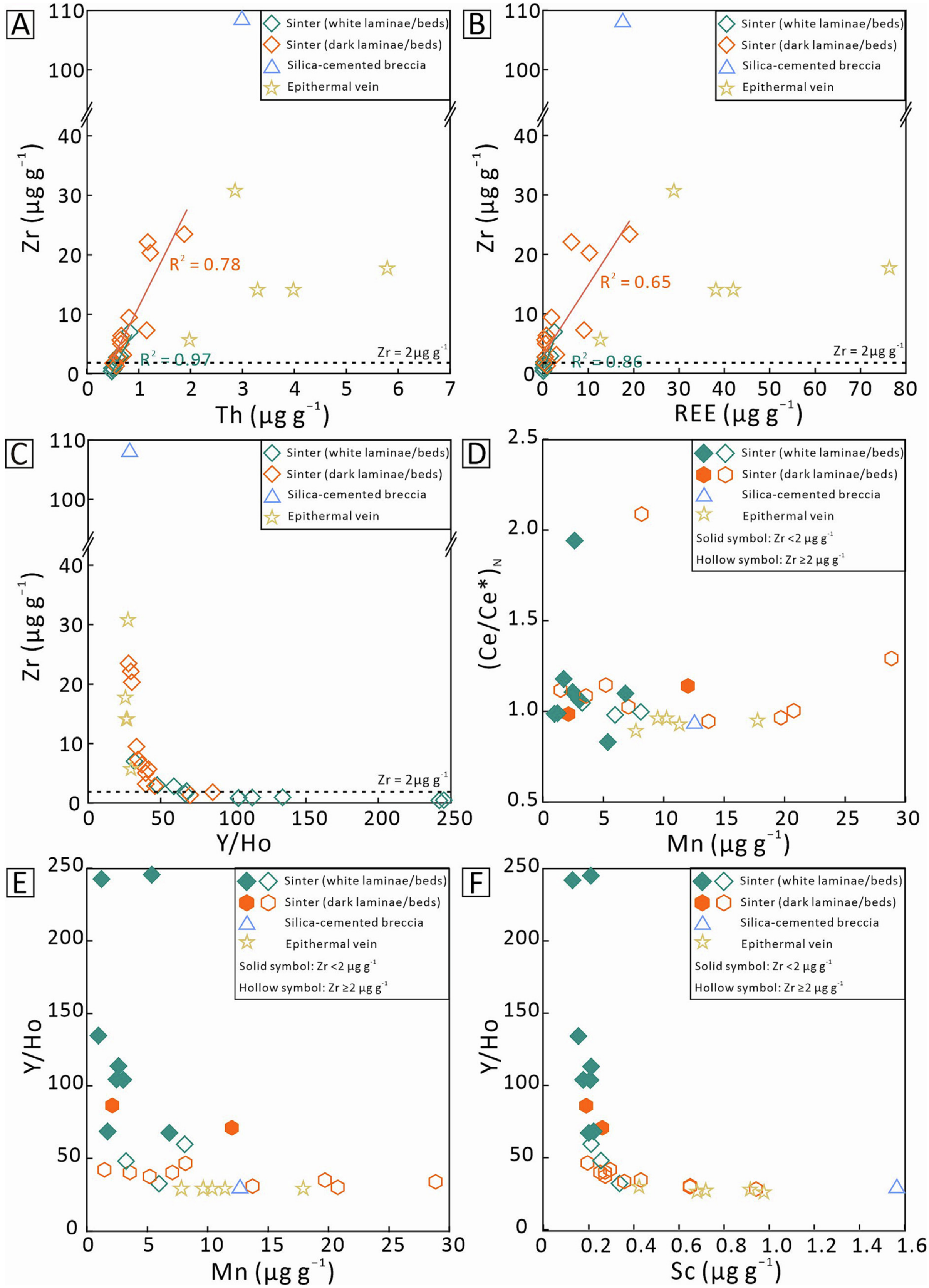

Fig. 8. Plots of (A) Zr vs. Th; (B) Zr vs. ΣREE; (C) Zr vs. Y/Ho; (D) $(Ce/Ce^*)_N$ vs. Mn; (E) Y/Ho vs. Mn; and (F) Y/Ho vs. Sc of the laminated to thinly bedded sinter, silica-cemented breccia and epithermal veins. Note: the studied sinter with solid symbols (Zr <2 μg g^{-1}) and hollow symbols (Zr ≥2 μg g^{-1}) is shown in Panels D to F. The unit of Zr, Th, ΣREE, Mn and Sc contents is μg g^{-1}.

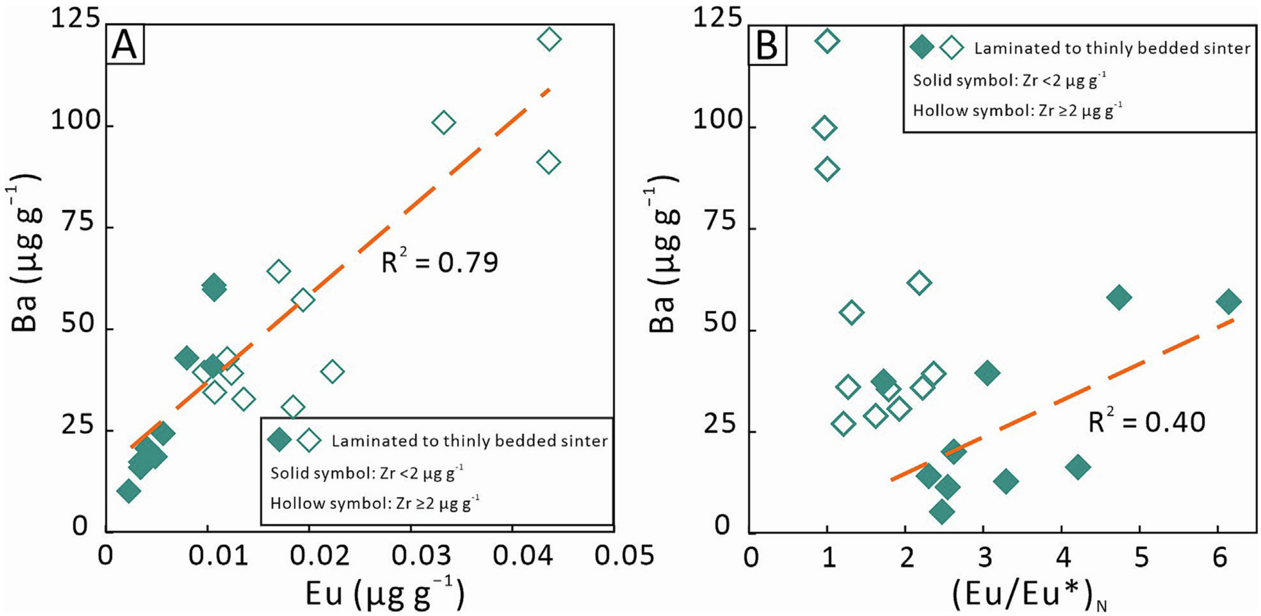

Fig. 9. Plots showing (A) Ba vs. Eu contents (μg g^{-1}) and (B) Ba contents (μg g^{-1}) vs. $(Eu/Eu^*)_N$ in the sinter samples. A strong linear relationship is present in the Ba vs. Eu content (μg g^{-1}) plot, and a weak linear relationship is observed in the Ba content (μg g^{-1}) vs. $(Eu/Eu^*)_N$ plot. One sample with a very high Ba content is excluded. Note: the studied sinter with solid symbols (Zr <2 μg g^{-1}) and hollow symbols (Zr ≥2 μg g^{-1}) is shown in Panels A and B.

range from 5.93 to 39.04 μg g^{-1}, from 0.95 to 3.94 μg g^{-1}, from 2.73 to 28.42 μg g^{-1}, from 1.07 to 3.70 μg g^{-1} and from 66.17 to 225.09 μg g^{-1}, respectively.

5. Interpretation and discussion

5.1. Interpretation of $^{87}Sr/^{86}Sr$ ratios

Hot spring deposits, including both sinter and travertine, have been found to record $^{87}Sr/^{86}Sr$ ratios of the underlying reservoir rocks (González-Guzmán et al., 2022; Luo et al., 2024). Thus, the $^{87}Sr/^{86}Sr$ ratios of siliceous sinter are expected to overlap with those of the corresponding reservoir rocks. However, if an exogenous substance is introduced into the sinter during its deposition, such as lithic or volcaniclastic sediments, the measured $^{87}Sr/^{86}Sr$ of the sinter may not reliably indicate the $^{87}Sr/^{86}Sr$ signatures of the reservoir rocks (Luo et al., 2024). Thus, an evaluation of detrital $^{87}Sr/^{86}Sr$ contamination was undertaken in this study by examining the $^{87}Sr/^{86}Sr$–Sr, $^{87}Sr/^{86}Sr$–Zr and $^{87}Sr/^{86}Sr$–ΣREE relationships of the sinter (Fig. 6A, B and C). Epigenous detritus, which is derived from mechanical and chemical processes acting on pre-existing rocks at the surface, typically has significantly higher Sr and Zr contents and ΣREE values than 'clean' sinter (Luo et al., 2024). Thus, detrital $^{87}Sr/^{86}Sr$ contamination, if present, would likely cause increases in Sr, Zr, and ΣREE, and would be expected to be associated with $^{87}Sr/^{86}Sr$ increases or decreases. With respect to the studied K_1x laminated/bedded sinter and epithermal veins, no strong $^{87}Sr/^{86}Sr$–Sr, $^{87}Sr/^{86}Sr$–Zr and $^{87}Sr/^{86}Sr$–ΣREE correlations were observed (Fig. 6A, B and C), despite some samples (especially epithermal veins) displaying very high values of Zr and ΣREE (Fig. 6A and B). This finding suggests that detrital contamination, even if occurring in some samples, may have a minimal impact on the $^{87}Sr/^{86}Sr$ of the studied sinter.

The measured $^{87}Sr/^{86}Sr$ values of the Wugonglilu and Sipingshan sinters fall almost within the $^{87}Sr/^{86}Sr$ range of the T_3dj (marine) siliceous rock, instead of the $^{87}Sr/^{86}Sr$ range of the K_1d rhyolite (Table 1, Fig. 5A). However, this does not mean that the Sr of the sinter mainly originates from the T_3dj (marine) siliceous rock, but rather that the sinter is too old to ignore the influence of the radioactive decay of ^{87}Rb to ^{87}Sr (Banner, 1995). Therefore, the initial $^{87}Sr/^{86}Sr$ of the sinter (i.e. here termed $(^{87}Sr/^{86}Sr)_i$, and referring to the $^{87}Sr/^{86}Sr$ of the sinter during its deposition in the Early Cretaceous; 106 ± 3 Ma) was computed (Table A2). Furthermore, the $^{87}Sr/^{86}Sr$ of potential Sr source rocks in the Early Cretaceous (i.e. designated here as $(^{87}Sr/^{86}Sr)_{cre}$) was also calculated (Table A2). Results show that the laminated/bedded sinter and epithermal veins have very uniform $(^{87}Sr/^{86}Sr)_i$, from 0.7066469 ± 0.00012 to 0.711076 ± 0.000113, and fall into the $(^{87}Sr/^{86}Sr)_{cre}$ of the K_1d rhyolite. However, the $(^{87}Sr/^{86}Sr)_i$ of over half of the samples overlaps with the $(^{87}Sr/^{86}Sr)_{cre}$ of the T_3dj (marine) siliceous rock (Fig. 5B). These results suggest that both the marine siliceous rock unit and the rhyolite are possible Sr sources of the sinter.

Given the above analysis, it is challenging to determine whether the main source of Sr in the sinter was the T_3dj marine siliceous rock unit or the K_1d rhyolite. With respect to the rhyolite, it is stratigraphically positioned beneath the sinter and has a thickness of >100 m. During deposition of the studied sinter, the rhyolite was probably widely distributed in/near the study area, constituting the main rock outcrops in recharge areas and/or serving as the main rock type within the geothermal reservoirs. In this case, the rhyolite may have supplied a significant amount of Sr to the thermal fluids depositing the studied sinter during infiltration and percolation of meteoric water and convective rising upflow of heated groundwater within the reservoirs. In contrast, siliceous rocks are generally not ideal reservoir rocks due to their low porosity and permeability (e.g., Behl and Smith, 1992; Matysik et al., 2021). However, the T_3dj (marine) siliceous rock unit is highly fractured and brecciated, and is also extensively distributed in/near the study area (Fig. A1). The formation of abundant fractures would promote the migration and storage of thermal fluids within the T_3dj (marine) siliceous rock unit. A broadly analogous occurrence is the Miocene Monterey Formation, a siliceous marine sedimentary rock that is a highly fractured petroleum source rock in California, USA (e.g., Finkbeiner et al., 1997; Dholakia et al., 1998). Similarly, the marine siliceous unit in the study area might have functioned as a geothermal reservoir rock during the Cretaceous. Furthermore, the T_3dj marine siliceous rock unit is stratigraphically positioned beneath the K_1d rhyolite. Thus, if the Cretaceous geothermal reservoirs were hosted in the marine siliceous rock unit, higher reservoir temperatures may have been present owing to a higher geothermal gradient deeper in

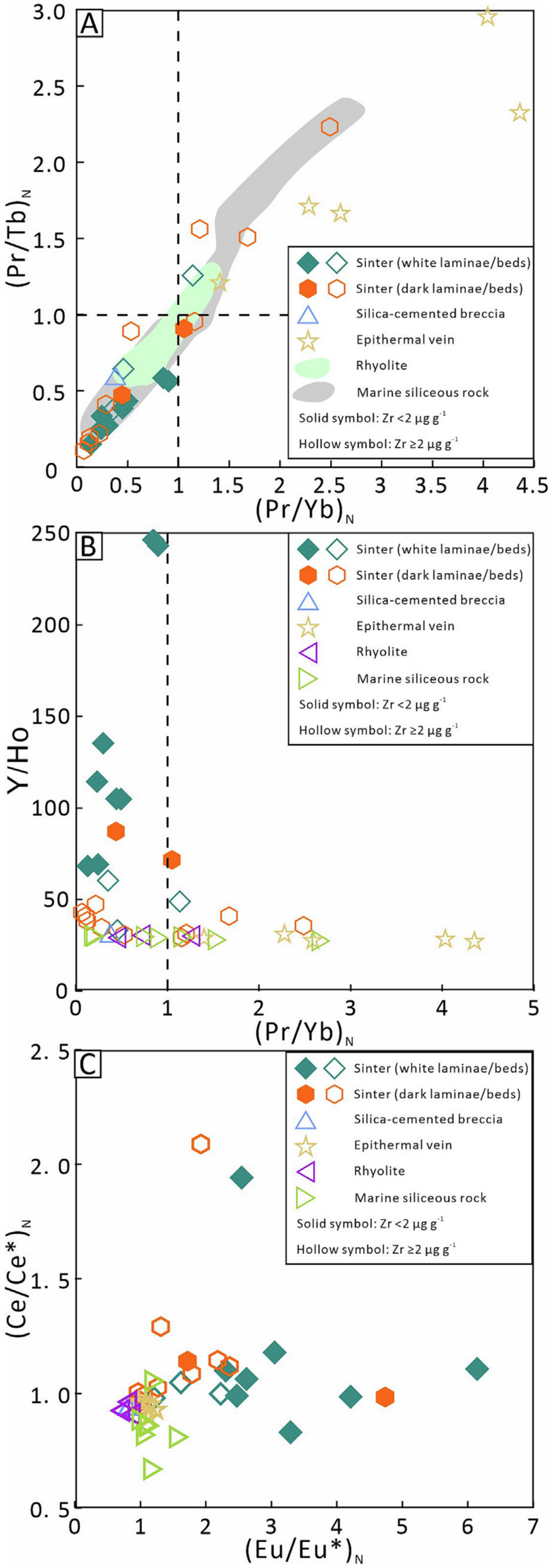

Fig. 10. Plots of (A) $(Pr/Tb)_N$ vs. $(Pr/Yb)_N$; (B) Y/Ho vs. $(Pr/Yb)_N$; and (C) $(Ce/Ce^*)_N$ vs. $(Eu/Eu^*)_N$ of the investigated rocks. Solid symbols indicate samples with Zr <2 μg g^{-1}; hollow symbols indicate samples with Zr ≥2 μg g^{-1}.

the crust. The potentially elevated temperatures also could have enhanced dissolution of the marine siliceous host rocks (e.g., Tester et al., 1994; Dove, 1999; Van de Kamp, 2008) and contributed to the enrichment of dissolved silica in the paleo-spring waters forming the studied sinter.

5.2. Interpretation of REE + Y data

5.2.1. Contamination of original trace element signatures

The REE + Y signature of sinter deposits has been found to be susceptible to contamination by exogenous substances (i.e. minerals or sediments carried by water or wind from other locations), particularly terrestrial detritus (Luo et al., 2024). In addition, Fe–Mn oxide, sulfide, and phosphate are also potential REE + Y contaminants. The concentrations of some elements, such as Zr and Th, are useful indicators of contamination by terrestrial detritus (e.g., Webb and Kamber, 2000; Frimmel, 2009; Meng et al., 2019; Gong et al., 2021; Zhao et al., 2021; Zhao et al., 2022), as detrital materials usually contain higher Zr and Th concentrations as well as ΣREE greater than hot spring siliceous deposits (e.g., Uysal et al., 2011; Feng et al., 2014; Hamilton et al., 2019b; Churchill et al., 2021). Strong positive linear Th–Zr (R^2 = 0.97) and ΣREE–Zr correlations (R^2 = 0.86) were observed in the Wugonglilu white and dark sinter laminae/beds (Th–Zr: R^2 = 0.78; ΣREE–Zr: R^2 = 0.65) (Fig. 8A and B). This finding indicates that detrital REE + Y contamination masks the original depositional REE + Y signatures of the Wugonglilu sinter. Such contamination is also supported by the Y/Ho–Zr relationship of the studied sinter: samples with Zr >3 μg g^{-1} have very low Y/Ho ratios (typically <40) (Fig. 8C). This is because the terrestrial detritus, such as eroded and transported rhyolite, can display very low Y/Ho ratios (e.g., Bau, 1996; Pack et al., 2007; Uysal et al., 2011; Zhao et al., 2022). Thus, to further analyze the REE + Y signatures of the studied sinter, samples with strong detrital REE + Y contamination must be excluded. In this study, a Zr concentration threshold of 2 μg g^{-1} was used to categorize the samples into those with significant REE + Y contamination (Zr ≥2 μg g^{-1}) and those that are more pristine (Zr <2 μg g^{-1}).

In general, contamination by secondary Fe–Mn oxides and sulfide can be evaluated by examining the Mn and Fe contents of the deposits and their relationships with Y/Ho and $(Ce/Ce^*)_N$ (e.g., Bolhar and Van Kranendonk, 2007; Bau and Koschinsky, 2009; Tang et al., 2013; Adebayo et al., 2020; Zhao et al., 2022), and by evaluating the chalcophile elements (e.g., Pb and Sc) of the deposits and their correlations with Y/Ho (e.g., Bolhar and Van Kranendonk, 2007; Bolhar et al., 2015), respectively. The studied samples with Zr <2 μg g^{-1} display very low contents of Mn (usually <10 μg g^{-1}) and Sc (<0.3 μg g^{-1}) and no clear Mn–$(Ce/Ce^*)_N$, Mn–Y/Ho, or Sc–Y/Ho relationships (Fig. 8D–F). Therefore, significant Fe–Mn oxide and sulfide contamination to the Wugonglilu sinter can be ruled out. The phosphate content of the studied sinter was not measured, but data from Han et al. (2023) show that the P_2O_5 of the Sipingshan Formation siliceous rock at Sipingshan (2 km distance from Wugonglilu) is below 0.01 %. Additionally, the phosphorus content of sinter is generally <25 μg g^{-1} (e.g., Feng et al., 2014). These reports suggest that phosphate, if present, is probably in low concentrations in sinter in the region and had no influence on the REE + Y values of these sinters.

5.2.2. REE + Y signatures in the studied sinter

The studied sinter samples with Zr <2 μg g^{-1} exhibit very high Y/Ho values, weak to no Ce anomalies, significant positive Eu anomalies, and LREE-depletion relative to both MREE and HREE. The Y/Ho ratio of sinter deposits has been shown to be controlled by the differential adsorption of Ho and Y onto mineral surfaces, and also due to the formation of Fe–Mn (oxyhydr)oxides (Luo et al., 2024). As to the studied epithermal system, oxic conditions were not present during the migration of thermal fluids within the reservoir and during thermal fluid upwelling. This is because pyrite, which forms in reducing conditions (e.g., Berner, 1984; Graham and Ohmoto, 1994; Möller and Kersten, 1994; Jones et al., 2005), was observed within the epithermal veins and also in the laminated/bedded sinter at Wugonglilu and Sipingshan (e.g., Sun et al., 2012; Zhang et al., 2013; Zhang, 2014; Wang et al., 2022; Han et al., 2023; He et al., 2023). Therefore, it is suggested that no Fe–Mn oxides were formed along the subsurface migration pathways of the upflowing thermal fluid that fed the Cretaceous hot springs forming the studied sinter, suggesting no influence of Fe–Mn oxides on the Y/Ho ratio. Comparatively, the preferential absorption of Ho onto mineral surfaces is very common and almost inevitable during groundwater migration (e.g., Bau, 1999; Möller, 2002a; Bau and Koschinsky, 2009; Siebert et al., 2014), and is thus considered to play an important role in causing the high Y/Ho in the studied sinter, which is significantly higher than the Y/Ho of the T_3dj marine siliceous rock and the K_1d rhyolite (Table 1 and Figs. 8C and 10B). The absence of subsurface Fe–Mn oxides also excludes their influence on the $(Ce/Ce^*)_N$ of the sinter. In this study, the $(Ce/Ce^*)_N$ values of many sinter samples fall within the $(Ce/Ce^*)_N$ ranges of the marine siliceous rock unit and the rhyolite (Fig. 10C), and similar good $(Ce/Ce^*)_N$ correspondence was also observed in sinter from Rehai (China) (Luo et al., 2024). Thus, the $(Ce/Ce^*)_N$ of sinter is often inherited from its reservoir rocks (Luo et al., 2024).

A remarkable REE + Y feature of the Wugonglilu sinter is the strong positive Eu anomaly (1.72 to 6.14, Figs. 7A, 9B and 10C, Table 1) compared to both PAAS and potential reservoir rocks. Generally, a strong positive Eu anomaly in sedimentary rocks is attributed to (1) Eu^{2+} transferred into the hydrothermal fluids due to Eu-rich mineral dissolution, especially plagioclase, during host rock leaching through infiltration and circulation of thermal fluids (e.g., Lewis et al., 1997; Möller, 2000; Möller, 2002b; Sanada et al., 2006; Uysal et al., 2011); and (2) the reduction of Eu^{3+} to Eu^{2+} ions under extremely reducing conditions at temperatures >250 °C (e.g., Sverjensky, 1984; Bau, 1991; Möller, 2000; Möller, 2002b; Dai et al., 2016). However, the Eu values and Eu anomalies are incorrect in samples with high Ba/Eu (e.g., Ba/Eu > 1000; Loges et al., 2012b), due to interferences by BaO and/or BaOH during ICP-MS analysis (e.g., Dulski, 1994; Wang et al., 2012; Dekov et al., 2015; Chang et al., 2019; Djokic et al., 2020). Indeed, the concentrations of Ba and Eu in the Wugonglilu sinter samples show a significant linear correlation ($R^2 = 0.79$), with Ba/Eu ratios ranging from 1673 to 5714 (Fig. 9A). Thus, the unusually high $(Eu/Eu^*)_N$ in the Wugonglilu sinter might imply spectral interference of Ba on Eu. Such interference is also confirmed in the Ba–Eu anomaly plot (Fig. 9B). The least contaminated sinter samples (with low Zr contents, especially Zr <2 μg g^{-1}) have the highest Eu anomalies and display a weak linear Ba–$(Eu/Eu^*)_N$ relationship ($R^2 = 0.4$). This is because the sinter samples with minimal contamination have very low concentrations of rare earth elements, making the contribution of BaO to Eu more pronounced. Therefore, the presence of barium (Ba), which has a much higher concentration than Eu, undermines the reliability of the Eu analyses in our study area.

The sinter samples with Zr <2 μg g^{-1} are characterized by significant depletion of LREE compared to both MREE and HREE (usually $(Pr/Tb)_N \le 0.5$; $(Pr/Yb)_N \le 0.9$; Fig. 10A, B), closely resembling the $(Pr/Tb)_N$ and $(Pr/Yb)_N$ signatures of the T_3dj marine siliceous rock unit and the K_1d rhyolite (Fig. 10A, B). However, it must be noted that most of the studied sinter samples are significantly depleted in LREE (i.e., $(Pr/Tb)_N$ and $(Pr/Yb)_N$ below 0.5; Fig. 10A); whereas, many samples of the marine siliceous rock unit and the rhyolite exhibit only slight LREE-depletion to significant LREE-enrichment (i.e., $(Pr/Tb)_N$ and $(Pr/Yb)_N$ over 0.5). These comparisons suggest that the PAAS-normalized LREE-depletion of the studied sinter samples may not be influenced only by the overall REE + Y pattern of the reservoir rock(s). Similar LREE-depletion compared to reservoir rock was also observed in sinter from Rehai and was interpreted to be controlled by the formation of strong HREE–carbonate complexes within the groundwater (Luo et al., 2024). This mechanism can be applied here as well. Although the studied sinter was formed in the Cretaceous, hydro-chemical studies on hot springs undergoing active sinter deposition have revealed a high content of HCO_3^- (e.g., Liao and Zhao, 1999; Guo and Wang, 2012; Yan et al., 2021). As a result, strong HREE–carbonate complexes (dominantly $Ln(CO_3)_2^-$) are expected to be formed in many sinter-deposition hot spring systems, including the Wugonglilu sinter.

5.3. Depositional environment of the Wugonglilu sinter

Siliceous deposits can accumulate from both subaerial and subaqueous hot springs (e.g., Canet et al., 2005; Guido and Campbell, 2012; Dekov et al., 2015; Des Marais and Walter, 2019; Hamilton et al., 2019c; Renaut and Owen, 2023). The Cretaceous rocks in the study area and nearby regions were formed in terrestrial sedimentary or volcanic settings (e.g., Yang et al., 2013b; Zhang, 2014; Han et al., 2023; He et al., 2023); thus, a submarine origin can be ruled out.

Nevertheless, the origin of the K_1x sinter (also called siliceous rock on geologic maps and in previous literature) at Wugonglilu and nearby regions remains unclear. Previous studies interpreted the sinter as a deposit of subaerial hot springs (Sun et al., 2012), but recently Han et al. (2023) proposed a sublacustrine spring origin of these siliceous deposits. In general, siliceous thermal spring-related deposits have been widely observed in geothermal systems in both subaerial and sublacustrine environments (e.g., Guido and Campbell, 2014; Liao, 2018; Des Marais and Walter, 2019; You et al., 2019; Renaut and Owen, 2023). However, the two depositional environments display notably different characteristics of laminated/bedded siliceous deposits. Subaerial laminated to bedded sinter has been widely observed in terrestrial volcanic environments, and accumulates large and extensive sinter apron terraces, extending to hundreds of meters and reaching up to several tens of meters in thickness, and contains highly variable morphologies of microbial textures (e.g., Campbell et al., 2015b; Jones and Peng, 2015; Campbell et al., 2019; Hamilton et al., 2019c). In contrast, sublacustrine laminated siliceous deposits usually consist of thin (<5 mm), finely laminated, discontinuous crusts of silica, and are more limited areally, extending laterally for several meters and only up to decimeters in thickness (e.g., Renaut et al., 2002; Renaut and Owen, 2023). The epigean (i.e. on land surface), K_1x laminated to thinly bedded sinter of this study contains alternating, centimeter-scale, dark and white layers that can extend at least 200 m along hillslopes and are up to 20 m thick, significantly different from the less texturally diverse, laminated hydrothermal silica deposits known from sublacustrine settings.

The fabric, microbial and mineral composition of the Wugonglilu sinter is notably distinct from those of sublacustrine siliceous deposits. Typically, siliceous deposits in sublacustrine environments are massive and structureless, lacking distinctive textures such as geyserite and terraces that are commonly associated with subaerial settings (e.g., Renaut et al., 2002; Guidry and Chafetz, 2003; Jones et al., 2007). In contrast, the Wugonglilu siliceous sinter exhibits characteristics (see Figs. 3, 4 and 2A) akin to those observed in modern and ancient terrestrial siliceous hot spring settings. For example, small domal (Fig. 3A, B), columnar/digitate (Fig. 3H and Fig. A2B) and cumulate to pseudocolumnar stromatolites (Fig. 3I), and palisade fabrics (Figs. 3C, D and A2A) were identified. Additionally, a stratigraphic transition (Fig. A2B) in the sinter from palisade fabrics to digitate, spicular features was also observed. Such features typically represent the product of shifting channels and pools within subaerial hot spring settings. Unlike typical sublacustrine siliceous deposits, which often contain filamentous and coccoid microbes, sponges, and lacustrine diatoms, our analysis revealed an absence of sponges and lacustrine diatoms in the sinter. The mineral composition of the Wugonglilu laminated/bedded sinter predominately comprises 98 % to 99 % quartz (e.g., Zhang, 2009; Sun et al., 2012; Wang et al., 2022), highlighting its significant siliceous composition, a feature not universally found in lake deposits. Moreover, no evidence of silica chimneys, commonly found in lacustrine environments, was observed in this area (e.g., Xu et al., 2005; Zhang, 2009, 2014; Huang et al., 2010; Sun et al., 2012; Quan and Dong, 2013; Zhang et al., 2013). Furthermore, the presence of gold mineralization beneath the sinter bolsters the evidence for the subaerial geothermal origin of the K_1x laminated to thinly bedded sinter. This is because epithermal gold deposits are often associated with siliceous sinter, with gold largely depositing in veins in the subsurface and the sinters forming at the surface (e.g., Hamilton et al., 2019b, and references therein). In summary, such evidence strongly suggests that the siliceous deposits in the study area more likely originated in a subaerial hot-spring setting.

5.4. Cause(s) of sinter lamination: constraints from trace elemental analysis

The laminated to thinly bedded horizons of the Wugonglilu sinter are marked by alternating dark and white laminae/beds. Rapid vs. slow evaporation/precipitation has been proposed to explain the alternating dark laminae (composed of "wet" opal) and light (or white) laminae (constituting "dry" opal) deposited in modern hot spring vent areas and pools (e.g., Jones and Renaut, 2004; Campbell et al., 2015a). In spicular geyserite, a specific type of siliceous sinter formed in high-temperature (>70 °C), near-vent areas, such alternating dark and white laminae occur only within the cores of these textures, and each lamina is very thin (500 nm to 4 μm thick) (e.g., Walter et al., 1996; Jones and Renaut, 2003; Lowe and Braunstein, 2003; Jones and Renaut, 2004; Campbell et al., 2015a). In addition, microbial mats are absent in the alternating dark and white laminae of geyserite (e.g., Walter, 1976b; Jones and Renaut, 2004) and rather very thin biofilms are sometimes preserved (Guido et al., 2019). These literature examples are very different from the studied laminated and thinly bedded sinter at Wugonglilu, which was deposited in mound slope environments of lower temperature (~60–40 °C) geothermal settings, based on the diverse microbial textures preserved there, instead of high-temperature spring vent areas (~75–100 °C; cf. Cady and Farmer (1996)).

The systematic alternation between the white microbe-deficient and dark microbe-rich laminae/beds of the studied sinter implies that the precipitation of the two types of laminae/beds is related to a cyclic process. Konhauser et al. (2001) advocated that the lamination in sinter deposits was determined by the competition between silicification of microbes (i.e. silica precipitation rate) and microbial growth. When the silica precipitation rate is significantly higher than the microbial growth rate (i.e. microbes cannot keep pace with silicification), then microbe-deficient laminae/beds would be expected to be formed (and vice versa). Thus, any processes which can cause significant cyclic changes of the silica precipitation rate and microbial growth rate are likely to affect the formation of white and dark laminae/beds in mid- to low-temperature sinter apron deposits.

The water discharge (i.e., volumetric flow rate) of hot springs is not stable and is related to changing geothermal reservoir conditions. For example, water discharge changes of hot springs, affecting water levels and temperatures on an approximately monthly cycle, have been reported for the Waimangu–Rotomahana–Tarawera geothermal field (New Zealand) (e.g., Vandemeulebrouck et al., 2008; Ward et al., 2017). Moreover, different water discharge rates, volume and duration may cause significant changes of the silica precipitation rate and further govern the microbial growth rate (e.g., Walter, 1976a; Cady and Farmer, 1996). Thus, if the change of geothermal reservoir conditions was very regular in the studied system, cyclic dark and white laminae/beds would be formed. However, this mechanism cannot explain the difference of elemental Zr, Th, and ΣREE (i.e. elements enriched in exogenous detritus) between the dark and white laminae/beds in the studied sinter, because deep-seated reservoir condition changes would not deposit exogenous detritus during subaerial sinter formation. Besides, regular variations of deep reservoir conditions are rare, as they are often induced by fault activities which are typically rather sudden and unpredictable (e.g., Foxford et al., 1998; Kim et al., 2003).

Seasonal contrasts in the weather, especially the number of hours of sunlight and amount of rainfall, have been considered to have a significant impact on the development of white microbe-deficient and dark microbe-rich laminae (Jones and Peng, 2015). Jones and Peng (2015) argued that the growth of microbes (e.g., *Calothrix*) thrived during the dry season when sunlight was at its maximum and there was less water discharging from springs due to seasonal drops in the water table. Conversely, the growth and activities of *Calothrix* were diminished in the wet season when sunlight was reduced, and the microbes were affected by the considerable and combined water flow from the spring, rain and run-off. As a result, the microbe-rich laminae and microbe-deficient laminae in the Meinuquan sinter studied by Jones and Peng (2015) were interpreted to have formed in the dry season and wet season, respectively. The dark lamina/beds in the Wugonglilu laminated to thinly bedded sinter typically exhibit higher Zr, Th, and ΣREE contents than the white laminae/beds (Figs. 7A and 8A–C). This indicates that the dark microbe-rich laminae/beds were largely formed under conditions with more exogenous detrital influxes, whereas the white microbe-deficient laminae/beds were deposited from geothermal fluids with little to no detrital inputs. Theoretically, exogenous detritus could have been introduced into the studied system by aeolian or rainfall activities.

Aeolian activity can erode and transport materials (such as soil, sand and dust) from surrounding areas onto the hot spring system. Such aeolian activity is more pronounced in the dry season (e.g., Wishman, 1990; Forman et al., 2005). Additionally, the dry season is often accompanied by longer hours of sunlight per day. In this case, laminae formed during the dry season might be microbe-rich, with high concentrations of exogenous detritus due to the high growth rates of microbes and strong aeolian activity. In contrast, microbe-poor laminae with low concentrations of exogenous detritus could largely be formed in the wet season, because the influx of rainwater slows down the silica precipitation rate, and shorter hours of sunlight per day impede microbial growth. This interpretation aligns partially with the model proposed by Jones and Peng (2015) and could explain the alternation of dark and white laminae/beds in the studied sinter. However, it must be noted that silica precipitation is inhibited in the wet season (due to the dilution of spring water), leading to the expectation that microbe-poor white laminae would be thinner than the microbe-rich dark laminae. This contrasts with the observed pattern in the studied bedded sinter, which generally displays thick white laminae/beds and thin dark laminae (Fig. 2A). Therefore, the hypothesis of aeolian activity-controlled detritus input seems less plausible.

In addition to aeolian activity, exogenous detritus can be supplied by rainfall activity and associated runoff. Compared with the dry season, the wet season is characterized by markedly greater rainfall activity. In this circumstance, the dark laminae/beds and the white laminae/beds of the studied sinter are expected to have been deposited in the wet and dry seasons, respectively. The Wugonglilu laminated to thinly bedded sinter stands out owing to its centimeter-scale layers, significantly thicker than the millimeter-scale laminae of the Meinuquan sinter (Jones and Peng, 2015). Therefore, the studied sinter was primarily deposited at a high rate (several centimeters per year) from physical pulses/flow of thermal fluid discharge. In this context, during the dry season (Fig. 11A), there could have been less microbial development because the sinter precipitation rate might have been too high to offer suitable conditions for microbial colonization. During the wet season (Fig. 11B), excess surface water generated by rainfall events may have entered the geothermal area. This could have led to both the deposition of detritus onto the sinter apron surface and the dilution of thermal spring waters. The latter would make the spring water less saturated with respect to amorphous SiO_2 and would decrease the silica precipitation rate, forming laminae/beds thinner than those formed in the dry season. The silica precipitation rate decline would also allow the microbial growth rate to surpass the silicification rate and thus the microbes could have been preserved under these conditions. Consequently, the sinter laminae/beds formed in the wet season are dark, microbe-rich, and thin. In summary, the laminae/beds of the Wugonglilu sinter appear to have been controlled by seasonal

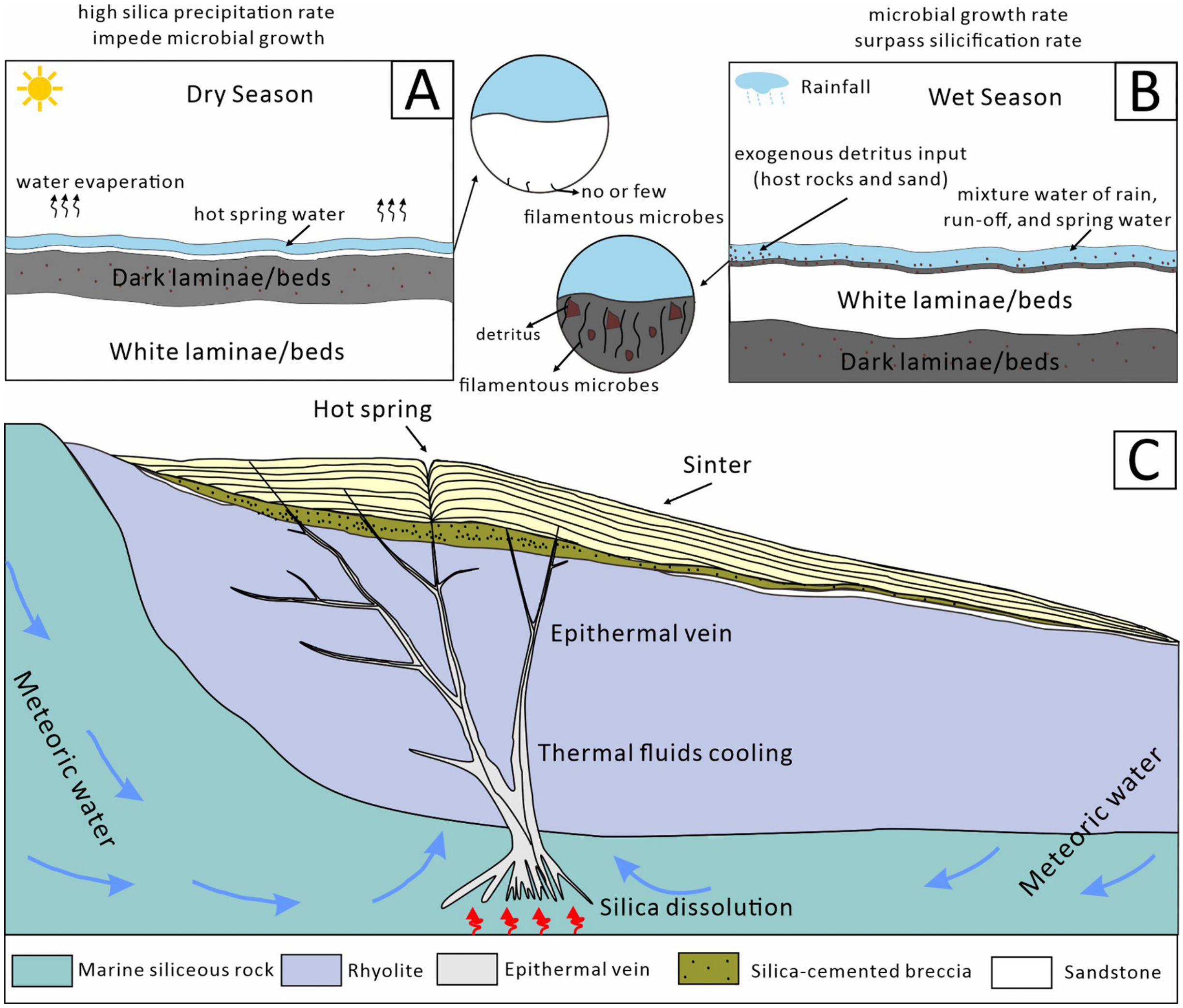

Fig. 11. (A–C) Formation model of the Wugonglilu sinter. (A) and (B) represent the formation of white and dark laminae/beds in the Wugonglilu, respectively.

climate fluctuations, with the crucial factor being the amount of rainwater (i.e. rainfall) input, not aeolian activity.

5.5. Sinter formation model

The formation of siliceous sinter is strictly associated with hot springs that are mainly composed of silica-rich, near-neutral pH, alkali chloride fluids, which originate from a deep geothermal reservoir (e.g., Fournier, 1985b; Ünal Ercan et al., 2022; Brogi et al., 2023). Studies have shown that the upwelling and circulation of fluids in a paleo-geothermal system are closely related to the development of faults (e.g., Taillefer et al., 2017; Hamilton et al., 2019c; Olvera-García et al., 2020; Brogi et al., 2023). During the Cretaceous Period, as the Paleo-Pacific plate continued to subduct beneath the East Asian continent, tectonic and magmatic disruption in the study area were frequent (e.g., Zhang, 2009; Sun et al., 2012; Zhang et al., 2013; Tang et al., 2016; Han et al., 2023; Liang et al., 2023), generating geothermal gradients and an enormous number of fractures in the marine siliceous rock unit and the rhyolite.

Meteoric waters infiltrated from porous sediments and fractured rocks of the recharge area and were heated and pressurized in the geothermal reservoir(s) composed of the marine siliceous rock unit and/or the rhyolite. The elevated water temperatures promoted water–rock interactions within the reservoir(s) and increased the concentration of dissolved SiO_2 in the thermal fluids. As pressurized thermal fluids migrated beneath the study area, permeable faults and fractures, created by tectonic and magmatic activities, channeled fluid upflow from shallow geothermal reservoir(s), leading to the formation of silica-rich hot springs. During the early stages of hot spring activity, substantial sinter deposits might not have developed; instead, silica-cemented breccia might have been formed. This occurred because sudden hydrothermal eruptions might have happened with sudden pressure drop in the system, perhaps owing to seismic or volcanic activity, and flashing steam to the fracturing and accumulation of brecciated host rocks and sandstone at the surface (e.g., Browne and Lawless, 2001; Montanaro et al., 2024). These deposits were initially unconsolidated, containing high porosity and well-developed cavities, making them ideal for infiltration and percolation of silica-rich hot spring water. As these clastic deposits became cemented by silica, their porosity and permeability gradually diminished. Consequently, substantial deposition of laminated to thinly bedded sinter on a nearly horizontal or slightly inclined surface commenced from nearby vent-spring discharge areas, forming a shield-like sinter deposit (Fig. 11C). Near-surface conduits were locations of epithermal vein formation, and gradually became sealed due to ongoing silica precipitation, but multiple stages of tectonic and magmatic activity generated additional tectonic fractures and faults, leading to the cross-cutting of epithermal veins (Fig. 11C).

6. Conclusions

This study investigated the $^{87}Sr/^{86}Sr$, REE + Y, and sedimentological characteristics of the Cretaceous sinter at Wugonglilu, NE China, and compared these features with its (potential) bedrock units. Laminated to thinly bedded sinter, silica-cemented breccia and epithermal veins are the primary lithofacies. Distinctive features of the laminated to thinly bedded sinter, including particular microbial fabrics, and porous to dense, centimeter-scale layering, reflect that the sinter was deposited from subaerial hot springs. The uniform $^{87}Sr/^{86}Sr$ ratios of the sinter are similar to those of nearby K_1d rhyolite and T_3dj marine siliceous rock, and imply that they might be the silica sources of the sinter. Detrital REE + Y contamination was observed in the studied sinter. The dark laminae/beds typically exhibit higher concentrations of Zr, Th, and ΣREE compared to the white laminae/beds. This contrast suggests that the white laminae/beds were deposited with little detrital input and the dark laminae/beds were formed under conditions with more detritus influx (i.e. wet season). The sinter samples with less detrital contamination (Zr <2 μg g^{-1}) exhibit $(Eu/Eu^*)_N > 2$ and $Y/Ho > 60$, which are significantly higher than the K_1d rhyolite and T_3dj siliceous rock unit. Nonetheless, such positive Eu and Y anomalies might be caused by the spectral interference of Ba on Eu and the preferential absorption of Ho onto mineral surfaces during groundwater migration, respectively. Many of the studied sinter samples show similar $(Ce/Ce^*)_N$ to the bedrock units, suggesting that the $(Ce/Ce^*)_N$ of the sinter was largely inherited from them. The distribution patterns of REE + Y in the studied sinter show a predominance of depletion in the LREE, whereas the samples of the marine siliceous rock unit and the rhyolite mainly exhibit only slight LREE-depletion to significant LREE-enrichment. This might be attributed to the formation of strong HREE–carbonate complexes in the paleofluids. In this contribution, the importance of combining geochemical and sedimentological research in the study of fossil sinter was highlighted, thereby increasing our understanding of the genesis of fossil siliceous sinter and the geochemical connections between siliceous sinter and reservoir rock(s).

Supplementary data to this article can be found online at https://doi.org/10.1016/j.sedgeo.2024.106618.

CRediT authorship contribution statement

Yaxian You: Writing – review & editing, Writing – original draft, Software, Methodology, Investigation, Conceptualization. **Huaguo Wen:** Supervision, Conceptualization. **Lianchao Luo:** Writing – review & editing, Supervision, Methodology, Investigation, Conceptualization. **Kathleen A. Campbell:** Writing – review & editing, Supervision, Conceptualization. **Diego M. Guido:** Writing – review & editing, Supervision, Conceptualization. **Enrico Capezzuoli:** Writing – review & editing, Supervision. **Zhipeng Lu:** Writing – review & editing, Methodology, Investigation. **Lei Du:** Writing – review & editing, Investigation. **Yunbao Yang:** Writing – review & editing, Investigation.

Data availability

Data will be made available on request.

Declaration of competing interest

The authors declare that they have no known competing financial interests or personal relationships that could have appeared to influence the work reported in this paper.

Acknowledgments

This study was financially supported by the National Natural Science Foundation of China (grant no. 41972116) and the Natural Science Foundation of Sichuan Province (grant no. 2022NSFSC1075). Funding for K. Campbell's contributions to the research was from the Royal Society of New Zealand Marsden Fund (Project ID: 17-UOA-037). The authors acknowledge Ms. Di Yang (Chengdu University of Technology) for her help in Sr isotope analyses.

References

Adebayo, S.B., Cui, M., Hong, T., Akintomide, O., Kelly, R.P., Johannesson, K.H., 2020. Rare earth element cycling and reaction path modeling across the chemocline of the Pettaquamscutt River estuary, Rhode Island. Geochimica et Cosmochimica Acta 284, 21–42.

Antonelli, M.A., Pester, N.J., Brown, S.T., DePaolo, D.J., 2017. Effect of paleoseawater composition on hydrothermal exchange in midocean ridges. Proceedings of the National Academy of Sciences 114, 12413–12418.

Awramik, S.M., Grey, K., 2005. Stromatolites: biogenicity, biosignatures, and bioconfusion. In: Hoover, Richard B., Levin, Gilbert V., Rozanov, Alexei Y., Gladstone, G. Randall (Eds.), Astrobiology and Planetary Missions. Proceedings of SPIE, Bellingham, WA (USA) vol. 5906, pp. 227–235 (September).

Banner, J.L., 1995. Application of the trace element and isotope geochemistry of strontium to studies of carbonate diagenesis. Sedimentology 42, 805–824.

Bau, M., 1991. Rare-earth element mobility during hydrothermal and metamorphic fluid–rock interaction and the significance of the oxidation state of europium. Chemical Geology 93, 219–230.

Bau, M., 1996. Controls on the fractionation of isovalent trace elements in magmatic and aqueous systems: evidence from Y/Ho, Zr/Hf, and lanthanide tetrad effect. Contributions to Mineralogy and Petrology 123, 323–333.

Bau, M., 1999. Scavenging of dissolved yttrium and rare earths by precipitating iron oxyhydroxide: experimental evidence for Ce oxidation, Y–Ho fractionation, and lanthanide tetrad effect. Geochimica et Cosmochimica Acta 63, 67–77.

Bau, M., Koschinsky, A., 2009. Oxidative scavenging of cerium on hydrous Fe oxide: evidence from the distribution of rare earth elements and yttrium between Fe oxides and Mn oxides in hydrogenetic ferromanganese crusts. Geochemical Journal 43, 37–47.

Behl, R.J., Smith, B.M., 1992. Silicification of deep-sea sediments and the oxygen isotope composition of diagenetic siliceous rocks from the western Pacific, Pigafetta and east Mariana basins, LEG 129. Proceedings of the Ocean Drilling Program, Scientific Results 129, 37.

Berner, R.A., 1984. Sedimentary pyrite formation: an update. Geochimica et Cosmochimica Acta 48, 605–615.

Bolhar, R., Van Kranendonk, M.J., 2007. A non-marine depositional setting for the northern Fortescue Group, Pilbara Craton, inferred from trace element geochemistry of stromatolitic carbonates. Precambrian Research 155, 229–250.

Bolhar, R., Hofmann, A., Siahi, M., Feng, Y., Delvigne, C., 2015. A trace element and Pb isotopic investigation into the provenance and deposition of stromatolitic carbonates, ironstones and associated shales of the ~3.0Ga Pongola Supergroup, Kaapvaal Craton. Geochimica et Cosmochimica Acta 158, 57–78.

Bosak, T., Liang, B., Sim, M.S., Petroff, A.P., 2009. Morphological record of oxygenic photosynthesis in conical stromatolites. Proceedings of the National Academy of Sciences of the United States of America 106, 10939–10943.

Brogi, A., Israde, I., Árnadóttir, S., Capezzuoli, E., 2023. Tectonic control on travertine and silica sinter deposition in oceanic transform-fault setting: the case of the Lýsuskarð volcano-geothermal area, Snæfellsnes Peninsula, Iceland. International Geology Review 1–24.

Browne, P.R.L., Lawless, J.V., 2001. Characteristics of hydrothermal eruptions, with examples from New Zealand and elsewhere. Earth-Science Reviews 52, 299–331.

Cady, S.L., Farmer, J.D., 1996. Fossilization processes in siliceous thermal springs: trends in preservation along thermal gradients. In: Bock, G.R., Goode, J.A. (Eds.), Evolution of Hydrothermal Ecosystem on Earth (and Mars ?). Proceeding of the Ciba Foundation Symposium vol. 202. Wiley, Chivhester, U.K, pp. 150–173.

Campbell, K.A., Sannazzaro, K., Rodgers, K.A., Herdianita, N.R., Browne, P.R.L., 2001. Sedimentary facies and mineralogy of the Late Pleistocene Umukuri silica sinter, Taupo Volcanic Zone, New Zealand. Journal of Sedimentary Research 71, 727–746.

Campbell, K.A., Guido, D.M., Gautret, P., Foucher, F., Ramboz, C., Westall, F., 2015a. Geyserite in hot-spring siliceous sinter: window on Earth's hottest terrestrial (paleo)environment and its extreme life. Earth-Science Reviews 148, 44–64.

Campbell, K.A., Lynne, B.Y., Handley, K.M., Jordan, S., Farmer, J.D., Guido, D.M., Foucher, F., Turner, S., Perry, R.S., 2015b. Tracing biosignature preservation of geothermally silicified microbial textures into the geological record. Astrobiology 15, 858–882.

Campbell, K.A., Guido, D.M., John, D.A., Vikre, P.G., Rhys, D., Hamilton, A., 2019. The Miocene Atastra Creek sinter (Bodie Hills volcanic field, California and Nevada): 4D evolution of a geomorphically intact siliceous hot spring deposit. Journal of Volcanology and Geothermal Research 370, 65–81.

Campbell, K.A., Nicholson, K., Lynne, B.Y., Browne, P.R.L., 2020. 3D anatomy of a 60-year-old siliceous hot spring deposit at Hipaua–Waihi–Tokaanu geothermal field, Taupo Volcanic Zone, New Zealand. Sedimentary Geology 402, 105652.

Canet, C., Prol-Ledesma, R.M., Torres-Alvarado, I., Gilg, H.A., Villanueva, R.E., Cruz, R.L.-S., 2005. Silica-carbonate stromatolites related to coastal hydrothermal venting in Bahía Concepción, Baja California Sur, Mexico. Sedimentary Geology 174, 97–113.

Chang, C., Fu, Q., Wang, X., 2019. Linear correlation of Ba and Eu contents by hydrothermal activities: a case study in the Hetang Formation, South China. Geofluids 2019, 9797326.

Channing, A., Zamuner, A.B., ZúÑIga, A., 2007. A new Middle–Late Jurassic flora and hot spring chert deposit from the Deseado Massif, Santa Cruz province, Argentina. Geological Magazine 144, 401–411.

Cheng, Q., Ge, S.U.N., 2008. Late Cretaceous aquatic angiosperms from Jiayin, Heilongjiang, Northeast China. Acta Geologica Sinica - English Edition 82, 1133–1140.

Churchill, D.M., Manga, M., Hurwitz, S., Peek, S., Damby, D.E., Conrey, R., Wood, J.R., McCleskey, R.B., Keller, W.E., Hosseini, B., Hungerford, J.D.G., 2021. The structure and volume of large geysers in Yellowstone National Park, USA and the mineralogy and chemistry of their silica sinter deposits. Journal of Volcanology and Geothermal Research 419, 107391.

Dai, S., Graham, I.T., Ward, C.R., 2016. A review of anomalous rare earth elements and yttrium in coal. International Journal of Coal Geology 159, 82–95.
Davies, A.G.S., Cooke, D.R., Gemmell, J.B., van Leeuwen, T., Cesare, P., Hartshorn, G., 2008. Hydrothermal breccias and veins at the Kelian goldmine, Kalimantan, Indonesia: genesis of a large epithermal gold deposit. Economic Geology 103, 717–757.
Dekov, V.M., Lalonde, S.V., Kamenov, G.D., Bayon, G., Shanks, W.C., Fortin, D., Fouquet, Y., Moscati, R.J., 2015. Geochemistry and mineralogy of a silica chimney from an inactive seafloor hydrothermal field (East Pacific Rise, 18°S). Chemical Geology 415, 126–140.
Des Marais, D.J., Walter, M.R., 2019. Terrestrial hot spring systems: introduction. Astrobiology 19, 1419–1432.
Dholakia, S.K., Aydin, A., Pollard, D.D., Zoback, M.D., 1998. Fault-controlled hydrocarbon pathways in the Monterey Formation, California. AAPG Bulletin 82, 1551–1574.
Djokic, T., Van Kranendonk, M.J., Campbell, K.A., Havig, J.R., Walter, M.R., Guido, D.M., 2020. A reconstructed subaerial hot spring field in the ~3.5 billion-year-old Dresser Formation, North Pole Dome, Pilbara Craton, Western Australia. Astrobiology 21, 1–38.
Dove, P.M., 1999. The dissolution kinetics of quartz in aqueous mixed cation solutions. Geochimica et Cosmochimica Acta 63, 3715–3727.
Drake, B.D., Campbell, K.A., Rowland, J.V., Guido, D.M., Browne, P.R.L., Rae, A., 2014. Evolution of a dynamic paleo-hydrothermal system at Mangatete, Taupo Volcanic Zone, New Zealand. Journal of Volcanology and Geothermal Research 282, 19–35.
Dulski, P., 1994. Interferences of oxide, hydroxide and chloride analyte species in the determination of rare earth elements in geological samples by inductively coupled plasma-mass spectrometry. Fresenius' Journal of Analytical Chemistry 350, 194–203.
Eggins, S.M., Woodhead, J.D., Kinsley, L.P.J., Mortimer, G.E., Sylvester, P., McCulloch, M.T., Hergt, J.M., Handler, M.R., 1997. A simple method for the precise determination of ≥ 40 trace elements in geological samples by ICPMS using enriched isotope internal standardisation. Chemical Geology 134, 311–326.
Farmer, J.D., Des Marais, D.J., 1994. Biological versus inorganic processes in stromatolite morphogenesis: observations from mineralizing sedimentary systems. In: Stal, L.J., Caumette, P. (Eds.), Microbial Mats. Springer Berlin Heidelberg, Berlin, Heidelberg, pp. 61–68 (1994//).
Feng, J.-L., Zhao, Z.-H., Chen, F., Hu, H.-P., 2014. Rare earth elements in sinters from the geothermal waters (hot springs) on the Tibetan Plateau, China. Journal of Volcanology and Geothermal Research 287, 1–11.
Fernandez-Turiel, J.L., Garcia-Valles, M., Gimeno-Torrente, D., Saavedra-Alonso, J., Martinez-Manent, S., 2005. The hot spring and geyser sinters of El Tatio, Northern Chile. Sedimentary Geology 180, 125–147.
Finkbeiner, T., Barton, C.A., Zoback, M.D., 1997. Relationships among in-situ stress, fractures and faults, and fluid Flow: Monterey Formation, Santa Maria Basin, California. AAPG Bulletin 81, 1975–1999.
Forman, S.L., Marin, L., Pierson, J., Gomez, J., Miller, G.H., Webb, R.S., 2005. Aeolian sand depositional records from western Nebraska: landscape response to droughts in the past 1500 years. The Holocene 15, 973–981.
Fournier, R.O., 1985a. The behavior of silica in hydrothermal solutions. In: Berger, B.R., Bethke, P.M. (Eds.), Society of Economic Geologists, Geology and Geochemistry of Epithermal Systems. Reviews in Economic Geology vol. 2, pp. 45–62.
Fournier, R.O., 1985b. The Yellowstone magmatic–hydrothermal system, U.S.A. International Symposium on Geothermal Energy International 319–327 volume.
Fournier, R.O., Rowe, J.J., 1966. Estimation of underground temperatures from the silica content of water from hot springs and wet-steam wells. American Journal of Science 264, 685.
Foxford, K.A., Walsh, J.J., Watterson, J., Garden, I.R., Guscott, S.C., Burley, S.D., 1998. Structure and content of the Moab Fault Zone, Utah, USA, and its implications for fault seal prediction. Geological Society, London, Special Publications 147, 87–103.
Frimmel, H.E., 2009. Trace element distribution in Neoproterozoic carbonates as palaeoenvironmental indicator. Chemical Geology 258, 338–353.
Gong, Q., Li, F., Lu, C., Wang, H., Tang, H., 2021. Tracing seawater- and terrestrial-sourced REE signatures in detritally contaminated, diagenetically altered carbonate rocks. Chemical Geology 570, 120169.
González-Guzmán, R., Weber, B., Elabd, M.A., Solís, C., Bernard-Romero, R., Velasco-Tapia, F., Marín-Camacho, P., 2022. Petrogenesis of Holocene siliceous sinters from the Los Geysers geothermal field, northern Trans-Mexican Volcanic Belt. Journal of Volcanology and Geothermal Research 431, 107640.
Graham, U.M., Ohmoto, H., 1994. Experimental study of formation mechanisms of hydrothermal pyrite. Geochimica et Cosmochimica Acta 58, 2187–2202.
Guido, D.M., Campbell, K.A., 2009. Jurassic hot-spring activity in a fluvial setting at La Marciana, Patagonia, Argentina. Geological Magazine 146, 617–622.
Guido, D.M., Campbell, K.A., 2011. Jurassic hot spring deposits of the Deseado Massif (Patagonia, Argentina): characteristics and controls on regional distribution. Journal of Volcanology and Geothermal Research 203, 35–47.
Guido, D.M., Campbell, K.A., 2012. Diverse subaerial and sublacustrine hot spring settings of the Cerro Negro epithermal system (Jurassic, Deseado Massif), Patagonia, Argentina. Journal of Volcanology and Geothermal Research 229-230, 1–12.
Guido, D.M., Campbell, K.A., 2014. A large and complete Jurassic geothermal field at Claudia, Deseado Massif, Santa Cruz, Argentina. Journal of Volcanology and Geothermal Research 275, 61–70.
Guido, D.M., Channing, A., Campbell, K.A., Zamuner, A., 2010. Jurassic geothermal landscapes and fossil ecosystems at San Agustín, Patagonia, Argentina. Journal of the Geological Society 167, 11–20.
Guido, D.M., Campbell, K.A., Foucher, F., Westall, F., 2019. Life is everywhere in sinters: examples from Jurassic hot-spring environments of Argentine Patagonia. Geological Magazine 156, 1631–1638.
Guidry, S.A., Chafetz, H.S., 2002. Factors governing subaqueous siliceous sinter precipitation in hot springs: examples from Yellowstone National Park, USA. Sedimentology 49, 1253–1267.
Guidry, S.A., Chafetz, H.S., 2003. Anatomy of siliceous hot springs: examples from Yellowstone National Park, Wyoming, USA. Sedimentary Geology 157, 71–106.
Guo, Q., Wang, Y., 2012. Geochemistry of hot springs in the Tengchong hydrothermal areas, Southwestern China. Journal of Volcanology and Geothermal Research 215-216, 61–73.
Hamilton, A.R., Campbell, K.A., Rowland, J.V., Barker, S., Guido, D., 2019a. Characteristics and variations of sinters in the Coromandel Volcanic Zone: application to epithermal exploration. New Zealand Journal of Geology and Geophysics 62, 531–549.
Hamilton, A.R., Campbell, K.A., Rowland, J.V., Barker, S., Guido, D.M., 2019b. Fossilised geothermal surface features of the Whitianga Volcanic Centre (Miocene), Coromandel Volcanic Zone, New Zealand: controls and characteristics. Journal of Volcanology and Geothermal Research 381, 209–226.
Hamilton, A.R., Campbell, K.A., Guido, D.M., 2019c. Atlas of Siliceous Hot Spring Deposits (Sinter) and Other Silicified Surface Manifestations in Epithermal Environments. GNS Science, p. 56.
Han, S.-J., Yang, Y.-C., Bo, J.-W., Han, Z.-H., Huang, Y.-w., Yang, Y.-b., 2023. New insights into the genesis of the Sipingshan gold deposit in eastern Heilongjiang, north-eastern China: evidence from geology, U–Pb and Rb–Sr geochronology, geochemistry, and HOS-Pb isotopes. Ore Geology Reviews 154, 105325.
He, Y., Zhang, G., Yang, Y., Feng, Y., Kong, J., Chen, X., 2023. Genesis and tectonic setting of Sipingshan gold deposit in Nadanhada terrane, Sikhote-Alin orogenic belt: zircon U–Pb chronology, petrological and fluid geochemical constraints. Geoscience 1–28 (in Chinese with English abstract).
Huang, Y., Li, G., Lu, D., 2010. Prediction of deep orebody in Sipingshan gold deposit of Heilongjiang. Global Geology 29, 226–233 (in Chinese with English abstract).
Huenges, E., 2010. Geothermal Energy Systems: Exploration, Development and Utilization. Wiley, New Jersey (486 pp.).
Jones, B., Peng, X., 2015. Laminae development in opal-A precipitates associated with seasonal growth of the form-genus *Calothrix* (Cyanobacteria), Rehai geothermal area, Tengchong, Yunnan Province, China. Sedimentary Geology 319, 52–68.
Jones, B., Renaut, R.W., 1997. Formation of silica oncoids around geysers and hot springs at El Tatio, northern Chile. Sedimentology 44, 287–304.
Jones, B., Renaut, R.W., 2003. Petrography and genesis of spicular and columnar geyserite from the Whakarewarewa and Orakeikorako geothermal areas, North Island, New Zealand1. Canadian Journal of Earth Sciences 40, 1585–1610.
Jones, B., Renaut, R.W., 2004. Water content of opal-A: implications for the origin of laminae in geyserite and sinter. Journal of Sedimentary Research 74, 117–128.
Jones, B., Renaut, R.W., 2010. Impact of seasonal changes on the formation and accumulation of soft siliceous sediments on the discharge apron of Geysir, Iceland. Journal of Sedimentary Research 80, 17–35.
Jones, B., Renaut, R.W., Rosen, M.R., 1997a. Biogenicity of silica precipitation around geysers and hot-spring vents, North Island, New Zealand. Journal of Sedimentary Research 67, 88–104.
Jones, B., Rosen, M.R., Renaut, R.W., 1997b. Silica-cemented beachrock from Lake Taupo, North Island, New Zealand. Journal of Sedimentary Research 67, 805–814.
Jones, B., Renaut, R.W., Konhauser, K.O., 2005. Genesis of large siliceous stromatolites at Frying Pan Lake, Waimangu geothermal field, North Island, New Zealand. Sedimentology 52, 1229–1252.
Jones, B., De Ronde, C.E.J., Renaut, R.W., Owen, R.B., 2007. Siliceous sublacustrine spring deposits around hydrothermal vents in Lake Taupo, New Zealand. Journal of the Geological Society 164, 227–242.
Kelley, V.C., 1956. Thickness of strata. Journal of Sedimentary Research 26, 289–300.
Kim, C.J., Seung-Jae, L., Sang-Hee, K., 2003. Evaluation of feeder monitoring parameters for incipient fault detection using Laplace trend sta tistic. 38th IAS Annual Meeting on Conference Record of the Industry Applications Conference, 2003. 12–16 Oct. 2003 vol. 1282, pp. 1285–1291.
Kobare, N.D., Iskandar, I., Suryantini, 2023. Geochemical investigation on the implications of fluid origin, subsurface processes and recharge on the Tangkuban Perahu geothermal conceptual model. Geothermics 110, 102685.
Konhauser, K.O., Phoenix, V.R., Bottrell, S.H., Adams, D.G., Head, I.M., 2001. Microbial–silica interactions in Icelandic hot spring sinter: possible analogues for some Precambrian siliceous stromatolites. Sedimentology 48, 415–433.
Krings, M., 2021. Peculiar bundles and a knot of thin filaments in microbial mats from the Lower Devonian Rhynie and Windyfield cherts of Scotland. Review of Palaeobotany and Palynology 291, 104442.
Lawrence, M.G., Greig, A., Collerson, K.D., Kamber, B.S., 2006. Rare earth element and ettrium variability in South East Queensland waterways. Aquatic Geochemistry 12, 39–72.
Lewis, A.J., Palmer, M.R., Sturchio, N.C., Kemp, A.J., 1997. The rare earth element geochemistry of acid-sulphate and acid-sulphate-chloride geothermal systems from Yellowstone National Park, Wyoming, USA. Geochimica et Cosmochimica Acta 61, 695–706.
Liang, Y., Xu, Z., Zhou, J., Cheng, R., Wan, D., 2023. Subduction of the Palaeo-Pacific Plate beneath the Jiamusi Block: constraints from the Late Triassic–Late Jurassic sedimentary records in the eastern Jiamusi Block. Geological Journal 58, 1083–1100.
Liao, Z., 2018. Thermal springs and geothermal energy in the Qinghai–Tibetan Plateau and the surroundings. Springer, Singapore.
Liao, Z., Zhao, P., 1999. Yunnan–Tibet Geothemal Belt: Geothermal Resources and Case Histories. Science Press, Beijing (in Chinese with English abstract).
Loges, A., Wagner, T., Kirnbauer, T., Göb, S., Bau, M., Berner, Z., Markl, G., 2012a. Source and origin of active and fossil thermal spring systems, northern Upper Rhine Graben, Germany. Applied Geochemistry 27, 1153–1169.
Loges, A., Wagner, T., Barth, M., Bau, M., Göb, S., Markl, G., 2012b. Negative Ce anomalies in Mn oxides: the role of Ce^{4+} mobility during water–mineral interaction. Geochimica et Cosmochimica Acta 86, 296–317.

Lowe, D.R., Braunstein, D., 2003. Microstructure of high-temperature (>73 °C) siliceous sinter deposited around hot springs and geysers, Yellowstone National Park: the role of biological and abiological processes in sedimentation. Canadian Journal of Earth Sciences 40, 1611–1642.
Luo, L., Wen, H., Capezzuoli, E., Brogi, A., Liu, R., Vaselli, O., Wang, F., Lu, Z., You, Y., Kele, S., 2024. Strontium Isotopes and Rare-Earth Elements in Terrestrial Hot Spring Deposits: Characterization and Geothermal Implications (The manuscript has been submitted to Geological Society of America Bulletin for consideration).
Lynne, B.Y., 2012. Mapping vent to distal-apron hot spring paleo-flow pathways using siliceous sinter architecture. Geothermics 43, 3–24.
Lynne, B.Y., 2015. Impact of three common post-depositional environmental settings on siliceous sinter diagenesis: an eight year experiment. Journal of Volcanology and Geothermal Research 292, 84–101.
Lynne, B.Y., Campbell, K.A., 2003. Diagenetic transformations (opal-A to quartz) of low- and mid-temperature microbial textures in siliceous hot-spring deposits, Taupo Volcanic Zone, New Zealand. Canadian Journal of Earth Sciences 40, 1679–1696.
Lynne, B.Y., Campbell, K.A., James, B.J., Browne, P.R.L., Moore, J., 2007. Tracking crystallinity in siliceous hot-spring deposits. American Journal of Science 307, 612.
Matysik, M., Stemmerik, L., Olaussen, S., Rameil, N., Gianotten, I.P., Brunstad, H., 2021. Cherts, spiculites, and collapse breccias — porosity generation in upper Permian reservoir rocks, Gohta discovery, Loppa High, south-western Barents Sea. Marine and Petroleum Geology 128, 105043.
McKee, E.D., Weir, G.W., 1953. Terminology for stratification and cross-stratification in sedimentary rocks. GSA Bulletin 64, 381–390.
Meng, M., Liu, X., Fan, T., Duncan, I.J., 2019. Rare earth elements and yttrium (REY) geochemistry of reefal limestones in the Ordovician, Tarim Basin, NW China and their paleoenvironment implications. Acta Geologica Sinica - English Edition 93, 928–942.
Möller, P., 2000. Rare earth elements and yttrium as geochemical indicators of the source of mineral and thermal waters. In: Stober, I., Bucher, K. (Eds.), Hydrogeology of Crystalline Rocks. Springer Netherlands, Dordrecht, pp. 227–246.
Möller, P., 2002a. The distribution of rare earth elements and yttrium in water–rock interactions: field observations and experiments. In: Stober, I., Bucher, K. (Eds.), Water–Rock Interaction. Springer Netherlands, Dordrecht, pp. 97–123.
Möller, P., 2002b. Rare earth elements and yttrium in geothermal fluids. Water Science and Technology Library 97–125.
Möller, P., Kersten, G., 1994. Electrochemical accumulation of visible gold on pyrite and arsenopyrite surfaces. Mineralium Deposita 29, 404–413.
Möller, P., Dulski, P., Savascin, Y., Conrad, M., 2004. Rare earth elements, yttrium and Pb isotope ratios in thermal spring and well waters of West Anatolia, Turkey: a hydrochemical study of their origin. Chemical Geology 206, 97–118.
Montanaro, C., Cronin, S.J., Lerner, G.A., Simpson, M.P., Brooks-Clarke, I., Swanney, G., Milicich, S.D., Calibugan, A., Bardsley, C., Scheu, B., 2024. Natural processes leading to large, pre-historic hydrothermal eruptions in geothermal areas: Rotokawa geothermal field, New Zealand. GSA Bulletin 136, 27–56.
Olvera-García, E., Garduño-Monroy, V.H., Ostroumov, M., Gaspar-Patarroyo, T.L., Nájera-Blas, S.M., 2020. Structural control on hydrothermal upwelling in the Ixtlán de los Hervores geothermal area, Mexico. Journal of Volcanology and Geothermal Research 399, 106888.
Pack, A., Russell, S.S., Shelley, J.M.G., van Zuilen, M., 2007. Geo- and cosmochemistry of the twin elements yttrium and holmium. Geochimica et Cosmochimica Acta 71, 4592–4608.
Quan, C., Dong, D., 2013. Prospecting potentials in deep Sipingshan gold deposit, Hulin City, Heilongjiang Province. Gold 34, 19–23.
Ren, Y., Hao, Y., Wang, C., Quan, C., Li, J., Gao, Y., Shi, Y., 2020. Mineralization age, tectonic setting and material source of the gold–copper metallogeny in Wandashan area, Heilongjiang Province, NE China. Acta Petrologica Sinica 36 (3), 644–664.
Renaut, R.W., Owen, R.B., 2023. Spring deposits and hydrothermal alteration: records of hydrothermal activity in lake basins. In: Renaut, R.W., Owen, R.B. (Eds.), The Kenya Rift Lakes: Modern and Ancient: Limnology and Limnogeology of Tropical Lakes in a Continental Rift. Springer Berlin Heidelberg, Berlin, Heidelberg, pp. 77–127.
Renaut, R.W., Jones, B., Tiercelin, J.J., Tarits, C., 2002. Sublacustrine precipitation of hydrothermal silica in rift lakes: evidence from Lake Baringo, central Kenya Rift Valley. Sedimentary Geology 148, 235–257.
Renaut, R.W., Owen, R.B., Ego, J.K., 2017. Geothermal activity and hydrothermal mineral deposits at southern Lake Bogoria, Kenya Rift Valley: impact of lake level changes. Journal of African Earth Sciences 129, 623–646.
Rowland, J.V., Simmons, S.F., 2012. Hydrologic, magmatic, and tectonic controls on hydrothermal flow, Taupo Volcanic Zone, New Zealand: implications for the formation of epithermal vein deposits. Economic Geology 107, 427–457.
Sanada, T., Takamatsu, N., Yoshiike, Y., 2006. Geochemical interpretation of long-term variations in rare earth element concentrations in acidic hot spring waters from the Tamagawa geothermal area, Japan. Geothermics 35, 141–155.
Siebert, C., Möller, P., Geyer, S., Kraushaar, S., Dulski, P., Guttman, J., Subah, A., Rödiger, T., 2014. Thermal waters in the Lower Yarmouk Gorge and their relation to surrounding aquifers. Geochemistry 74, 425–441.
Sillitoe, R.H., 2015. Epithermal paleosurfaces. Mineralium Deposita 50, 767–793.
Simmons, S.F., White, N.C., John, D.A., 2005. Geological characteristics of epithermal precious and base metal deposits. In: Hedenquist, J.W., Thompson, J.F.H., Goldfarb, R.J., Richards, J.P. (Eds.), One Hundredth Anniversary Volume. Society of Economic Geologists, p. 0.
Sun, R., Bai, Z., Shi, J., Li, D., 2000. The genetical feature of the hot spring of Sipingshan gold deposit of Hulin city. Gold 21, 9–15.
Sun, J., Wang, L., Chi, X., Huang, Y., Quan, C., 2012. Geological characteristics and metallogenic model of Sipingshan hot spring type gold deposit in Hulin of Heilongjiang. Global Geology 31, 271–280 (in Chinese with English abstract).
Sverjensky, D.A., 1984. Europium redox equilibria in aqueous solution. Earth and Planetary Science Letters 67, 70–78.
Taillefer, A., Soliva, R., Guillou-Frottier, L., Le Goff, E., Martin, G., Seranne, M., 2017. Fault-related controls on upward hydrothermal flow: an integrated geological study of the Têt fault system, Eastern Pyrénées (France). Geofluids 2017, 8190109.
Tang, H.-S., Chen, Y.-J., Santosh, M., Zhong, H., Yang, T., 2013. REE geochemistry of carbonates from the Guanmenshan Formation, Liaohe Group, NE Sino-Korean Craton: implications for seawater compositional change during the Great Oxidation Event. Precambrian Research 227, 316–336.
Tang, J., Xu, W., Niu, Y., Wang, F., Ge, W., Sorokin, A.A., Chekryzhov, I.Y., 2016. Geochronology and geochemistry of Late Cretaceous–Paleocene granitoids in the Sikhote-Alin Orogenic Belt: petrogenesis and implications for the oblique subduction of the paleo-Pacific plate. Lithos 266-267, 202–212.
Taylor, S.R., McLennan, S.M., 1985. The Continental Crust: Its Composition and Evolution. Blackwell, Oxford.
Tester, J.W., Worley, W.G., Robinson, B.A., Grigsby, C.O., Feerer, J.L., 1994. Correlating quartz dissolution kinetics in pure water from 25 to 625°C. Geochimica et Cosmochimica Acta 58, 2407–2420.
Tobler, D.J., StefÁNsson, A., Benning, L.G., 2008. In-situ grown silica sinters in Icelandic geothermal areas. Geobiology 6, 481–502.
Ünal Ercan, H., Işık Ece, Ö., Schroeder, P.A., Gülmez, F., 2022. Characteristics and evolution of the Etili silica sinter epithermal deposits, Çanakkale — Turkey: relation to alkali chloride vs acid-sulfate fluids. Ore Geology Reviews 142, 104726.
Uysal, I.T., Gasparon, M., Bolhar, R., Zhao, J.-x., Feng, Y.-x., Jones, G., 2011. Trace element composition of near-surface silica deposits—a powerful tool for detecting hydrothermal mineral and energy resources. Chemical Geology 280, 154–169.
Van de Kamp, P.C., 2008. Smectite–illite–muscovite transformations, quartz dissolution, and silica release in shales. Clays and Clay Minerals 56, 66–81.
Van Kranendonk, M.J., 2011. Morphology as an indictor of biogenicity for 3.5–3.2 Ga fossil stromatolites from the Pilbara Craton, Western Australia. In: Reitner, J., Quéric, N.-V., Arp, G. (Eds.), Advances in Stromatolite Geobiology. Springer Berlin Heidelberg, Berlin, Heidelberg, pp. 537–554.
Vandemeulebrouck, J., Hurst, A.W., Scott, B.J., 2008. The effects of hydrothermal eruptions and a tectonic earthquake on a cycling crater lake (Inferno Crater Lake, Waimangu, New Zealand). Journal of Volcanology and Geothermal Research 178, 271–275.
Walter, M.R., 1976a. Hot-spring sediments in Yellowstone National Park. In: Walter, M.R. (Ed.), Developments in Sedimentology. Elsevier, pp. 489–498.
Walter, M.R., 1976b. Geyserites of Yellowstone National Park: an example of abiogenic "stromatolites". In: Walter, M.R. (Ed.), Developments in Sedimentology. Elsevier, pp. 87–112.
Walter, M.R., Desmarais, D., Farmer, J.D., Hinman, N.W., 1996. Lithofacies and biofacies of mid-Paleozoic thermal spring deposits in the Drummond Basin, Queensland, Australia. PALAIOS 11, 497–518.
Walter, M.R., McLoughlin, S., Drinnan, A.N., Farmer, J.D., 1998. Palaeontology of Devonian thermal spring deposits, Drummond Basin, Australia. Alcheringa: An Australasian Journal of Palaeontology 22, 285–314.
Wang, J., Chen, D., Wang, D.A.N., Yan, D., Zhou, X., Wang, Q., 2012. Petrology and geochemistry of chert on the marginal zone of Yangtze Platform, western Hunan, South China, during the Ediacaran–Cambrian transition. Sedimentology 59, 809–829.
Wang, W., Wei, H.-Z., Jiang, S.-Y., Tan, H.-B., Eastoe, C.J., Williams-Jones, A.E., Hohl, S.V., Wu, H.-P., 2019. The origin of rare alkali metals in geothermal fluids of southern Tibet, China: a silicon isotope perspective. Scientific Reports 9, 7918.
Wang, S., Sun, F., Wang, G., Liu, K., Liu, Y., 2022. Mineralization and genesis of Sipingshan gold deposit, Heilongjiang, China: evidence from ore deposit geology, geochemistry, ziron U–Pb ages, and H–O–S isotopes. Journal of Jilin University (Earth Science Edition) 52 (5), 1626–1648 (in Chinese with English abstract).
Ward, L., Taylor, M.W., Power, J.F., Scott, B.J., McDonald, I.R., Stott, M.B., 2017. Microbial community dynamics in Inferno Crater Lake, a thermally fluctuating geothermal spring. The ISME Journal 11, 1158–1167.
Watts-Henwood, N., Campbell, K.A., Lynne, B.Y., Guido, D.M., Rowland, J.V., Browne, P.R.L., 2017. Snapshot of hot-spring sinter at Geyser Valley, Wairakei, New Zealand, following anthropogenic drawdown of the geothermal reservoir. Geothermics 68, 94–114.
Webb, G.E., Kamber, B.S., 2000. Rare earth elements in Holocene reefal microbialites: a new shallow seawater proxy. Geochimica et Cosmochimica Acta 64, 1557–1565.
Wishman, E., 1990. Aeolian activity. A meteorological approach. Norwegian Archaeological Review 23, 105–113.
Xu, M., Yang, J., Lu, T., Jian, S., 2005. The characteristics and genesis analysis of Siping Mountain gold mine in Heilongjiang Province. Gold Science and Technology 13, 23–25 (in Chinese with English abstract).
Yan, Z., Xu, W., Luo, X., You, Y., Wen, H., 2021. Sedimentation sequence of a high-temperature silica-rich hot spring: evidence from isothermal evaporation experiments and from petrology and mineralogy of sinters. Carbonates and Evaporites 36, 29.
Yang, J., Wang, D., Zhang, W., 2013a. Occurrences of Early Cretaceous fossil woods in China: implications for paleoclimates. Palaeogeography Palaeoclimatology Palaeoecology 385, 213–220.
Yang, J., Zhao, Q., Zhang, J., 2013b. Preliminary study on the metallogenic model of Sipingshan hot-spring-type gold deposit in Hulin city. Science and Technology Innovation Herald 15, 113–114 (in Chinese with English abstract).
You, Y., Wen, H., Zheng, R., Luo, L., 2019. Advances and prospects of the terrestrial geothermal siliceous sinter research. Geological Science and Technology Information 38, 68–81.
Zhang, X., 2009. Study on Mineralization of Epithermal Gold Deposites in Eastern Heilongjiang, China: Take the Sishanlinchang and the Sipingshan Gold Deposits for Example. China University of Geolsciences (Master's thesis, 84 pp.).

Zhang, G., 2014. Study on Metallogenic System of Wandashan Massif, Eastern Heilongjiang Province. Jilin University, China (Ph.D. thesis, 179 pp.).
Zhang, G., Yang, Y., Wang, J., Wang, K., Ye, S., 2013. Geology, geochemistry, and genesis of the hot-spring-type Sipingshan gold deposit, eastern Heilongjiang Province, Northeast China. International Geology Review 55, 482–495.
Zhao, Y., Wei, W., Li, S., Yang, T., Zhang, R., Somerville, I., Santosh, M., Wei, H., Wu, J., Yang, J., Chen, W., Tang, Z., 2021. Rare earth element geochemistry of carbonates as a proxy for deep-time environmental reconstruction. Palaeogeography Palaeoclimatology Palaeoecology 574, 110443.
Zhao, Y., Wei, W., Santosh, M., Hu, J., Wei, H., Yang, J., Liu, S., Zhang, G., Yang, D., Li, S., 2022. A review of retrieving pristine rare earth element signatures from carbonates. Palaeogeography Palaeoclimatology Palaeoecology 586, 110765.